NASA Technical Memorandum 104566, Vol. 28

SeaWiFS Technical Report Series

Stanford B. Hooker, Editor
Goddard Space Flight Center
Greenbelt, Maryland

James G. Acker, Technical Editor
Hughes STX
Lanham, Maryland

Elaine R. Firestone, Technical Editor
General Sciences Corporation
Laurel, Maryland

Volume 28, SeaWiFS Algorithms, Part 1

Charles R. McClain, Kevin Arrigo, and Wayne E. Esaias
NASA Goddard Space Flight Center
Greenbelt, Maryland

Christopher W. Brown
National Research Council
Washington, D.C.

Michael Darzi and Frederick S. Patt
General Sciences Corporation
Laurel, Maryland

Robert A. Barnes
ManTech Environmental Technology, Inc.
Wallops Island, Virginia

Robert H. Evans and James W. Brown
University of Miami
Miami, Florida

Lakshmi Kumar
Hughes STX
Lanham, Maryland

National Aeronautics and
Space Administration

Goddard Space Flight Center
Greenbelt, Maryland 20771

1995

This publication is available from the NASA Center for AeroSpace Information,
800 Elkridge Landing Road, Linthicum Heights, MD 21090-2934, (301) 621-0390.

PREFACE

The scope of the SeaWiFS Calibration and Validation Program encompasses a very broad variety of topics, as evidenced in several previous volumes in the *SeaWiFS Technical Report Series*. Volume 28 further demonstrates the breadth and complexity of the issues that the program must address, and provides further justification for a comprehensive calibration and validation effort.

The chapters in this volume address operational algorithm issues, which include:

1) A description of the algorithms used in generating the level-2 masks and flags for each pixel, which are subsequently applied during the level-3 binning to exclude poor quality data;
2) An algorithm for masking ice- and cloud-contaminated pixels (also addressed in Chapter 1);
3) An algorithm for detecting pixels contaminated by coccolithophores (also addressed in Chapter 1);
4) An algorithm for removing out-of-band radiance from the observed radiances at each SeaWiFS band, due to the finite filter response functions across the visible and near-infrared spectrum; and
5) A description of the software routines for converting level-1a counts to level-1b calibrated radiances.

Greenbelt, Maryland
January 1995

—C. R. McClain

Table of Contents

ABSTRACT

This document provides five brief reports that address several algorithm investigations sponsored by the Calibration and Validation Team (CVT) within the Sea-viewing Wide Field-of-view Sensor (SeaWiFS) Project. This volume, therefore, has been designated as the first in a series of *algorithm* volumes. Chapter 1 describes the initial suite of *masks*, used to prevent further processing of contaminated radiometric data, and *flags*, which are employed to mark data whose quality (due to a variety of factors) may be suspect. In addition to providing the mask and flag algorithms, this chapter also describes the initial strategy for their implementation. Chapter 2 evaluates various strategies for the detection of clouds and ice in high latitude (polar and sub-polar regions) using Coastal Zone Color Scanner (CZCS) data. Chapter 3 presents an algorithm designed for detecting and masking coccolithophore blooms in the open ocean. Chapter 4 outlines a proposed scheme for correcting the out-of-band response when SeaWiFS is in orbit. Chapter 5 gives a detailed description of the algorithm designed to apply sensor calibration data during the processing of level-1b data.

Prologue

The purpose of the Sea-viewing Wide Field-of-view Sensor (SeaWiFS) Project is to obtain valid ocean color data of the world ocean for a five-year period, to process that data in conjunction with ancillary data to meaningful bio-optical fields [$K(490)$, chlorophyll a, and Coastal Zone Color Scanner (CZCS) pigment], and to make that data readily available to the user community through the GSFC DAAC. As part of this effort, the SeaWiFS Calibration and Validation Team (CVT) has three main tasks:

1) Calibration of the SeaWiFS instrument;
2) Development and validation of the operational atmospheric correction algorithm; and
3) Development and validation of the derived bio-optical algorithms and products.

Some of this work will be done internally at GSFC, while the remainder will be done externally at other institutions. NASA and the Project place the highest priority on assuring the accuracy of derived water-leaving radiances globally, and over the entire mission. These activities are discussed in detail in *The SeaWiFS Calibration and Validation Plan* (McClain et al. 1992).

Because many of the studies and development efforts under the auspices of the Calibration and Validation Program are not extensive enough to require dedicated volumes of the *SeaWiFS Technical Report Series*, the CVT has decided to publish volumes composed of brief, but topically specific, chapters. These volumes have been termed *Case Studies* and include Volumes 13, 19, and 27. Volume 28 deals with the mask and flag algorithms, the sensor calibration algorithm, and a sensor stray light correction algorithm. This volume, therefore, has been designated as the first in a series of *Algorithm* volumes.

The masks and flags are used in the level-2 processing for quality control. Masks identify pixels unsuitable for level-2 processing, e.g., land and clouds. Flags identify pixels where the bio-optical products may be of questionable validity, e.g., shallow water and coccolithophore blooms. The masks and flags are applied at the pixel level and are included in the level-2 products. They are also used in determining which pixels are included in the level-3 products. Most of the masks and flags are based on simple criteria, which are described in an overview chapter. More detailed discussions on the cloud and ice mask algorithm and the coccolithophore detection flag required separate chapters.

A short synopsis of each chapter in this volume is given below.

1. *SeaWiFS Quality Control Masks and Flags: Initial Algorithms and Implementation Strategy*

A variety of conditions related to geography, geometry, sensor response, and atmospheric and oceanic optical properties can render a pixel either inappropriate for processing to SeaWiFS level-2 geophysical values, or may cause the level-2 values to be of questionable validity. Incorporated into the level-2 processing scheme are 16 quality control (QC) masks and flags. *Masks* prevent the completion of data processing for affected pixels. *Flags* simply indicate that a quality test has failed, but processing of the data will continue. The results of these quality tests are stored within the level-2 products and can be displayed with the image data. The initial suite and the associated algorithms for the masks and flags are described.

2. *Cloud and Ice Detection at High Latitudes for Processing CZCS Imagery*

A cloud detection algorithm, which utilizes an albedo threshold at 750 nm (α_{750}), was tested on CZCS images of the Southern Ocean. It was found that reducing α_{750} from 1.6% to 0.9% resulted in a marked improvement in cloud detection, masking virtually all of the pixels with negative water-leaving radiances in the ice pack and along the edges of clouds. It was also found that this method was highly

sensitive to surface pressure, with a 2% change in pressure resulting in a change of up to 50% in computed pigment concentration, along with a large difference in the number of masked pixels. This method appears to perform well for both low and high reflectance waters, such as in the presence of a large coccolithophore bloom. Manipulating the value of α_{750} allowed masking of those pixels contaminated by sun glint. These results suggests that high latitude scenes previously rejected during the CZCS global processing may be salvaged by properly applying masks.

3. *Classification of Coccolithophore Blooms in Ocean Color Imagery*

Blooms of the coccolithophore *Emiliania huxleyi*, which occur in the surface layer of the ocean, are characterized by high ocean volume reflectance. This high reflectance biases the estimation of satellite-derived geophysical parameters, e.g., pigment concentration, that are based on water-leaving radiance measurements. To avoid erroneous estimates of geophysical parameters in the presence of blooms, it is desirable to implement a simple classification algorithm to flag their occurrence. The development of a supervised, multispectral classification algorithm is described in this chapter. The algorithm groups picture elements (pixels) of the imagery into coccolithophore *bloom* and *non-bloom* classes, based on the normalized water-leaving radiances of each pixel.

4. *A Proposed On-Orbit, Out-of-Band Correction Scheme for SeaWiFS*

Out-of-band responses for the eight SeaWiFS bands are elements of the instrument's radiometric calibration. In that calibration, the instrument views a broad area of known radiance, and the output from the bands are recorded in counts. The counts from each band include the out-of-band contribution, and these out-of-band contributions are functions of the spectral shape of the source that is measured. The SeaWiFS laboratory calibration, therefore, has the out-of-band correction for a 2,850 K source factored into its results. If the instrument measures a source with that particular spectral shape, those measurements automatically contain appropriate out-of-band corrections. The prelaunch calibration equations for SeaWiFS contain correction terms that convert the out-of-band responses from those for a 2,850 K source to those for a 5,900 K source. As a result, the SeaWiFS calibration equations now have the out-of-band correction for a 5,900 K source factored into them. The 5,900 K spectral shape closely duplicates the spectral shape for SeaWiFS ocean measurements. The errors arising from the use of the 5,900 K out-of-band corrections for ocean measurements are estimated to be small, on the order of a few tenths of a percent. If an alternate out-of-band correction is to be used, then the 5,900 K correction must be removed from the measurement results and a new out-of-band correction inserted in its place. An out-of-band correction based on the actual measurements from SeaWiFS, plus the procedure for its implementation, is presented here.

5. *Algorithm for the Application of the Sensor Calibration for SeaWiFS Level-2 Processing*

The processing of SeaWiFS level-1 data to level-2 requires that the sensor calibration be applied to the raw counts, prior to the derivation of geophysical values. The algorithm described herein is the implementation of the sensor calibration approach of Barnes et al. (1994b). The algorithm is designed for operational use by the SeaWiFS Project, and works on individual scan lines of SeaWiFS level-1a data, returning sensor-calibrated radiance values (level-1b data). Calibration data used in the calculations are stored in the *sensor calibration table*, which is also described.

Chapter 1

SeaWiFS Quality Control Masks and Flags: Initial Algorithms and Implementation Strategy

CHARLES R. MCCLAIN
Goddard Space Flight Center
Greenbelt, Maryland

ROBERT H. EVANS
JAMES W. BROWN
University of Miami
Miami, Florida

MICHAEL DARZI
General Sciences Corporation
Laurel, Maryland

ABSTRACT

A variety of conditions related to geography, geometry, sensor response, and atmospheric and oceanic optical properties can render a pixel either inappropriate for processing to SeaWiFS level-2 geophysical values, or may cause the level-2 values to be of questionable validity. Incorporated into the level-2 processing scheme are 16 QC masks and flags. *Masks* prevent the completion of data processing for affected pixels. *Flags* simply indicate that a quality test has failed, but processing of the data will continue. The results of these quality tests are stored within the level-2 products and can be displayed with the image data. The initial suite and the associated algorithms for the masks and flags are described.

1.1 INTRODUCTION

The SeaWiFS Project has been tasked by the Science Working Group (SWG) to provide highly accurate data products, e.g., water-leaving radiances to within ±5% and chlorophyll *a* to within ±35% (Hooker et al. 1992). To accommodate these goals, the SeaWiFS Project Calibration and Validation element has undertaken the tasks of identifying conditions that might produce spurious results, and defining the quantitative algorithms to test for each condition.

SeaWiFS will routinely collect global 4 km data. Much of the data, therefore, will be *contaminated* by cloud or land, i.e., the pixels will contain radiances reflected from either clouds or land masses, and for that reason these data will not be suitable for level-2 processing to SeaWiFS standard products (Firestone and Hooker 1995). Other conditions related to either the sensor performance, e.g., stray light, or optical properties in the atmosphere and ocean, e.g., high aerosol optical thickness and coccolithophore blooms, respectively, can cause the derived products to be of questionable validity. In many cases, algorithms for detecting these conditions have been developed; but in other cases, the algorithms require further development, e.g., dust aerosols (Carder et al. 1991 and Toratani and Fukushima 1993), and *Trichodesmium* blooms (Subramaniam and Carpenter 1994). In the latter case, these conditions are not explicitly included in the initial suite of quality control parameters.

The results from the global CZCS data processing project (Feldman et al. 1989) demonstrated that much care must be taken in data QC (McClain et al. 1992, McClain et al. 1993, and Evans and Gordon 1994). Despite the QC efforts undertaken during the CZCS global processing and the large percentage of rejected scenes, some erroneous data, e.g., cloud-contaminated data (Martin 1992), were approved and included in the level-3 products. The CZCS global processing QC protocols incorporated both automated techniques—primarily cloud, sensor ringing, and sun glint masks—and interactive QC techniques, i.e., visual screening of level-2 and level-3 products. The interactive evaluations were quite time-consuming and rather subjective, e.g., the anomalous water-leaving radiance category. The method also eliminated the entire scene if any portion of the scene appeared questionable, rather than rejecting data on a pixel-by-pixel basis. This approach

Table 1. SeaWiFS level-2 masks and flags.

Parameter	*Mask/Flag*	*Algorithm Name*	*Required Quantities*
Engineering Tolerance	Flag		32 *Red Limit* ranges.
Tilt	Flag		
Solar Zenith Angle	Flag	SOLZEN1	Maximum value.
Spacecraft Zenith Angle	Flag	SATZEN1	Maximum value.
High L_t [1]	Mask	HIGHLT1	8 *Knee* radiances.
Stray Light	Flag	STRAYLIGHT1	Number of along-track pixels.
			Number of along-scan pixels.
Missing Ancillary Data	Flag	ANCIL1	
Land	Mask	LAND1	Global land mask file.
Bathymetry	Flag	COASTZ1	Global 0–30 m depth mask file.
Clouds and Ice	Mask	CLDICE1	Albedo.
Sun Glint	Mask	SUNGLINT1	Fraction of $F_0(865)$. [2]
Atmospheric Correction Failure	Mask	EPSILON1	Acceptable range of ϵ values.
High $\tau_a(865)$ [3]	Flag	HIGHTAU1	Maximum value.
Negative $L_{WN}(\lambda)$ [4]	Flag	NEGLW1	
Low $L_{WN}(555)$	Flag	LOWLW1	Minimum value.
Coccolithophore	Flag	COCCOLITH1	Minimum $L_{WN}(443)$.
			Minimum $L_{WN}(555)$.
			$L_{WN}(2{:}5)$ range. [5]
			$L_{WN}(4{:}5)$ range. [5]
			$L_{WN}(2{:}4)$ range. [5]
Turbid Case-2 Water	Flag	TURBIDW1	Q factor value.
Chlorophyll Algorithm Failure	Flag	CHLOR1	$R_{rs}(1{:}3)$ range. [6]
			$R_{rs}(2{:}5)$ range. [6]

[1] Total radiance.
[2] Extraterrestrial solar irradiance.
[3] Aerosol radiance.
[4] Normalized water-leaving radiance.
[5] $L_{WN}(2{:}5) = L_{WN}(443)/L_{WN}(555)$: $L_{WN}(4{:}5) = L_{WN}(510)/L_{WN}(555)$: and $L_{WN}(2{:}4) = L_{WN}(443)/L_{WN}(510)$.
[6] $R_{rs}(1{:}3) = R_{rs}(412)/R_{rs}(443)$ and $R_{rs}(2{:}5) = R_{rs}(443)/R_{rs}(555)$, where R_{rs} is the remote sensing reflectance.

eliminated quite a bit of good data in order to avoid the inclusion of notably poor quality data in the level-3 fields.

The SeaWiFS QC methodology seeks to automate the testing so that interactive evaluations will be minimized. The masks and flags will be applied either on a line-by-line or a pixel-by-pixel basis, depending on the QC parameter. Masks prevent the completion of data processing for affected pixels, while flags simply indicate that a quality test has failed, but data processing will continue.

The results of each of the pixel-by-pixel tests will be preserved in the level-2 products as a 2-byte metadata field. This field, called `l2_flags`, is associated with each pixel, and each bit of `l2_flags` is assigned to a specific mask or flag. The line-by-line flag and mask information is saved in the level-2 file on a scan line-by-scan line basis, rather than on a pixel-by-pixel basis and, therefore, is not stored in the 16-bit quality field. These fields can be displayed separately. The mask and flag information is used in the level-3 processing to determine the quality of the binned data. How the flags and masks are applied in generating the level-3 products will be discussed in a separate document.

The definition and refinement of the QC parameter suite and the respective algorithms involved will be an continuing activity within the SeaWiFS Project. At each major reprocessing, the Project will have the opportunity to add and delete QC parameters, as well as update the algorithms.

1.2 MASKS AND FLAGS

Table 1 provides the list of initial mask and flag parameters, the algorithm names, and the required quantities to implement each criterion. The algorithm names are stored as attributes of the `l2_flags` field. Initially, there are two line-by-line flags, *Engineering Tolerance* and *Tilt*, which are generated by the *level-0 to level-1* conversion program. In this processing step, there are no line-by-line masks. In the case of masked pixels, the level-1 radiances are assigned to the level-2 normalized water-leaving radiance and aerosol radiance products, and a value of zero is assigned to the other products (i.e., pigment concentrations, diffuse attenuation, epsilon, and optical thickness fields).

1.2.1 Descriptions

Engineering Tolerance: A bit per scan line is reserved within the level-2 file, for each of 32 sensor engineering parameters, to indicate if the parameters are outside the normal operating range. These bits are stored, for level-2 as well as level-1a products, in a 4 byte metadata array associated with each scan line, called `eng_qual`. Table 2 provides the sensor engineering parameter operating ranges and *red limits*, i.e., values between which the instrument should normally operate.

Tilt: The scan line ranges for each tilt state (−20°, +20°, 0°, and tilting) are stored as metadata `tilt_ranges` and `tilt_flags` in the level-1a and level-2 products. In addition, the tilt angle (`tilt`) is stored as metadata for each scan line.

Solar Zenith Angle: All pixels having solar zenith angles greater than 70° will be flagged because of the uncertainty in atmospheric correction for large optical path lengths. Note also that as the angle of incidence exceeds 70°, the Fresnel reflectance increases rapidly, causing a corresponding limitation in the amount of radiation entering the water column.

Spacecraft (S/C) Zenith Angle: All pixels with pixel-to-spacecraft zenith angles greater than 45° will be flagged. Local area coverage (LAC) will extend to scan angles of 58.3°. The global area coverage (GAC) data recorded onboard will be truncated at scan angles of ±45°, although due to the Earth's curvature and sensor tilting, the S/C zenith angle will exceed 45° for GAC coverage along the edges of the scan. At 45°, the pixel area begins to increase rapidly as the scan angle is increased. At 45°, for example, the pixel area is increased by factors of about 2.5 (0° tilt) and 3.5 (20° tilt) over the pixel area at nadir, thus making interpretation of the products less definite. Large scan angles also increase the difficulty of both accurate navigation and atmospheric corrections. The CZCS data were limited to scan angles of ±39.34°, and the distortion at scan edges was considerable. Given the improved performance and navigation capabilities of SeaWiFS and SeaStar, respectively, it is felt that reasonable results should be attainable out to ±45°.

High L_t: All pixels having radiances less than the knee value in one or more bands will be flagged. Radiances above the knee in the bilinear gain are quantified at substantially lower precision than radiances below the knee (Barnes et al. 1994b). The reduction in precision ranges from 1:17 at 412 nm to 1:64 at 865 nm.

Stray Light: There are a number of sources of scattered light within the SeaWiFS sensor which cause light from adjacent pixels to contribute to the radiance of the pixel of interest (Barnes et al. 1994a). The problem is serious only in the vicinity of very bright pixels. The effect decreases to an acceptable level at about 4 GAC pixels in the scan direction and one GAC pixel along track, based on the prelaunch characterization data provided by Hughes Santa Barbara Research Center (SBRC). Due to the uncertainty in the exact location of the edge of the bright object in the GAC data, these are conservative values. The stray light flag will be applied to pixels adjacent to any pixel masked for high L_t.

Missing Ancillary Data: If a gap in the ancillary data exists, interpolated values will be used. This flag identifies where the gaps in the original data were located. Interpolation of ancillary data by the SeaWiFS Project should only be necessary for Television and Infrared Observation Satellite (TIROS) Operational Vertical Sounder (TOVS) ozone data which will be used if Total Ozone Mapping Spectrometer (TOMS) data are not available. The TOMS and the surface meteorological data (pressure, winds, relative humidity) are to be provided to the Project as global gridded fields.

Land: This criterion will apply to pixels completely or partially over land, as determined using a global land mask generated at the University of Miami.

Bathymetry: Pixels over water with depths shallower than, or equal to, 30 m will be flagged. A bathymetry flag file satisfying the depth criteria was generated using a global bathymetry database with a 5 minute spatial resolution. If a different depth threshold is to be used, a different global flag file must be generated and input to the level-2 processing program.

The purpose of this flag is to identify areas where bottom reflection may influence the water-leaving radiances, resulting in erroneous pigment concentration and diffuse attenuation estimates. Many coastal water masses possess sufficient clarity that this effect may be present. Using (1) (Gordon and Morel 1983),

$$K(440) = 0.0168 + 0.1031 C^{0.707}, \qquad (1)$$

where $K(440)$ is the diffuse attenuation coefficient at 440 nm, a 30 m penetration depth corresponds to C, a pigment concentration (chlorophyll a + phaeopigment) of only 0.08 mg m^{-3}, which should be sufficiently deep.

Clouds and Ice: Pixels having an albedo at 865 nm greater than 0.9% will be flagged (Arrigo and McClain 1995). The albedo computation accounts for the seasonal variations in solar zenith angle, and the use of 865 nm minimizes the influence of Rayleigh radiance and highly reflective oceanic waters which can occur with the presence of coccolithophore blooms and riverine sediment plumes.

Glint: Pixels having a glint radiance of $L_g(865)$ greater than $0.005F_0(865)$ will be masked. F_0 is the extraterrestrial solar constant adjusted for the Earth-sun distance. This formula is the expression used in the global CZCS processing (Evans and Gordon 1994). The expression for glint radiance (Viollier et al. 1980 and Gregg et al. 1993) is:

$$L_g(\lambda) = \frac{\rho T_0(\lambda,\theta_0) F_0(\lambda) P_W(\theta,\phi,\theta_0,\phi_0,W)}{4\cos\theta\cos^4\theta_n}. \qquad (2)$$

Table 2. Engineering telemetry parameters and scaling for SeaWiFS. The table includes absolute limits and *Red Limits* for the operation of SeaWiFS.

Analog Telemetry Point	*Conversion*		*Absolute Limits*		*Red Limits*	
	Slope	*Intercept*	*Low*	*High*	*Low*	*High*
Band 1/2 FPA[1] Temperature	−0.2667	66.667	−1.334	66.667	5.0	45.0
Band 3/4 FPA Temperature	−0.2667	66.667	−1.334	66.667	5.0	45.0
Band 5/6 FPA Temperature	−0.2667	66.667	−1.334	66.667	5.0	45.0
Band 7/8 FPA Temperature	−0.2667	66.667	−1.334	66.667	5.0	45.0
Telescope Motor Temperature	−0.2667	66.667	−1.334	66.667	5.0	45.0
Tilt Base Temperature	−0.2667	66.667	−1.334	66.667	5.0	45.0
Tilt Platform Temperature	−0.2667	66.667	−1.334	66.667	5.0	45.0
Half-Angle Motor Temperature	−0.2667	66.667	−1.334	66.667	5.0	45.0
Power Supply-A Input Current[2]	0.02	0.26	0.26	5.36	1.0	3.0
Power Supply-B Input Current[2]	0.02	0.26	0.26	5.36	1.0	3.0
+15 V Analog Power Voltage[3]	0.075	0.0	0.0	19.125	15.0	15.5
−15 V Analog Power Voltage[3]	−0.075	0.0	−19.125	0.0	−15.5	−15.0
+5 V Logic Power Voltage[3]	0.025	0.0	0.0	6.375	4.9	5.6
Power Supply Temperature	−0.2667	66.667	−1.334	66.667	5.0	45.0
B1/B2 Post-Amplifier Temperature	−0.2667	66.667	−1.334	66.667	5.0	45.0
Servo Driver Temperature	−0.2667	66.667	−1.334	66.667	5.0	45.0
+30 V Servo Power Voltage[3]	0.15	0.0	0.0	38.25	28.5	31.0
+21 V Servo Power Voltage[3]	0.1044	0.0	0.0	26.622	20.0	22.0
−21 V Servo Power Voltage[3]	−0.1044	0.0	−26.622	0.0	−22.0	−20.0
+5 V Servo Power Voltage[3]	0.025	0.0	0.0	6.375	4.9	5.6
Angular Momentum Speed[3,4]	8.52	−377.0	−377.0	1795.6	1215.0	1255.0
Tilt Platform Position[3]	1.44	0.0	0.0	367.2	0.0	360.0
Tilt Base Position[3]	1.44	0.0	0.0	367.2	0.0	360.0
+28 V Heater Power[3]	0.14	0.0	0.0	35.7	27.0	29.0
Telescope-A Motor Current[3,5]	0.0024	0.0	0.0	0.612	0.1	0.4
Telescope-B Motor Current[3,5]	0.0024	0.0	0.0	0.612	0.1	0.4
Half-Angle-A Motor Current[3,5]	0.0024	0.0	0.0	0.612	0.1	0.4
Half-Angle-B Motor Current[3,5]	0.0024	0.0	0.0	0.612	0.1	0.4
Servo-A Phase Error[3,5]	0.01	−1.25	−1.25	1.25	−1.0	1.0
Servo-B Phase Error[3,5]	0.01	−1.25	−1.25	1.25	−1.0	1.0
Angular Momentum Compensation A-Motor Current[3,4,5]	0.016	0.0	0.0	4.08	0.08	0.6
Angular Momentum Compensation B-Motor Current[3,4,5]	0.016	0.0	0.0	4.08	0.08	0.6

1. Focal Plane Assembly
2. This parameter is dependent upon the choice of power supply. (It does not appear in the instrument discrete telemetry, so it is assumed to be a spacecraft field.)
3. This parameter is dependent upon the analog power *on*.
4. This parameter is dependent upon the angular momentum compensation *on*.
5. This parameter is dependent upon the choice of servo-A or -B.

In this expression, ρ represents the Fresnel reflectivity, and P_W is the probability of seeing sun glint in the spacecraft direction (θ, ϕ), when the wind speed is W and the sun position is (θ_0, ϕ_0), as described by Cox and Munk (1954). The total downward transmittance of irradiance is represented by T_0, and θ_n is defined as

$$\theta_n = \arccos\left(\frac{\cos\theta + \cos\theta_0}{2\cos\omega}\right), \quad (3)$$

where

$$\cos 2\omega = \cos\theta\cos\theta_0 + \sin\theta\sin\theta_0\cos(\phi - \phi_0). \quad (4)$$

Atmospheric Correction Algorithm Failure: Pixels will be masked and assigned the level-1 total radiance values, where the atmospheric correction algorithm (Gordon and Wang 1994) fails to return ϵ values within a specified range. Strategies for using correction parameters from nearby pixels will be evaluated after launch.

High τ_a: Pixels having a $\tau_a(865)$ greater than a fixed threshold will be flagged. This flag is due to the fact that aerosol corrections become less reliable as atmospheric turbidity increases.

Negative L_W: Any pixel having a computed $L_W < 0$ will be flagged, and the normalized water-leaving value will be set to 0. Previous experience with CZCS data show that

negative radiances tend to occur in cloud shadows (Arrigo and McClain 1995), and can also occur when the water-leaving radiance is very small, such as in high pigment concentration Case-1 and turbid Case-2 waters.

Coccolithophore: Using a modified version of the method of Brown and Yoder (1994a) and Brown (1995), pixels selected as being contaminated by coccolithophores will be flagged. The primary modification to the Brown and Yoder (1994a) algorithm will be to delete the aerosol radiance $[L_a(670)]$ and *Bands Saturated* tests, which are not necessary with the pixel-by-pixel SeaWiFS processing. The *Bands Saturated* test was intended to mask data contaminated by sun glint in the CZCS global processing data products.

Low $L_{WN}(555)$: This flag denotes pixels where the normalized water-leaving radiance at 555 nm is below 0.21 $\mathrm{mW\,cm^{-2}\,\mu m^{-1}\,sr^{-1}}$, i.e., 75% of the clear water value (Gordon and Clark 1981). The *hinge point* (Duntley et al. 1974) in the water-leaving radiance spectrum is near 510 nm, so increases in pigment and particulate concentrations should increase the radiance above the clear water value. Any pixel with a water-leaving radiance value substantially below the clear water value represents an anomalous condition.

Turbid Case-2: The irradiance reflectance algorithm, recommended in Bricaud and Morel (1987) for discriminating between Case-1 and Case-2 waters, and updated in Morel (1988), will be used to flag Case-2 water. The condition for the limiting reflectance for Case-1 water at 555 nm is expressed as

$$R_{\mathrm{lim}}(555) = \frac{1 - 2.5B - \sqrt{(2.5B-1)^2 - 4.44B}}{2}, \quad (5)$$

where

$$B = \frac{0.33b}{K_d}. \quad (6)$$

The backscattering coefficient, b_b, is defined as

$$b_b(555) = 0.00075 + \left[0.0063 - 0.00263\log(C)\right]C^{0.62}, \quad (7)$$

and K_d is the diffuse attenuation coefficient for downwelling irradiance (Gordon and Morel 1983),

$$K_d(555) = 0.0717 + 0.039C^{0.64}. \quad (8)$$

Because the operational bio-optical algorithm (Carder pers. comm.) is based on R_{rs}, which is defined as the ratio of water-leaving radiance to surface downwelling irradiance, the turbid Case-2 flag will be set when R_{rs} exceeds a value analogous to R_{lim}, i.e.,

$$R_{rs}(555) > \frac{(1-\rho)R_{\mathrm{lim}}(555)}{Qn^2}, \quad (9)$$

where $Q = 3.42$ and the index of refraction $n = 1.341$. Note that $R_{rs}(\lambda) = L_{WN}(\lambda)/F_0(\lambda)$.

Chlorophyll Algorithm Failure: If the semi-analytic model for chlorophyll *a* (Carder pers. comm.) fails to return a valid value, a reflectance ratio algorithm will be used to compute chlorophyll *a*, and the pixel will be flagged.

Acknowledgments

The authors would like to thank Mike Jones, Eueng-nan Yeh, and Bob Barnes for their comments.

Chapter 2

Cloud and Ice Detection at High Latitudes for Processing CZCS Imagery

KEVIN R. ARRIGO
CHARLES R. MCCLAIN
Goddard Space Flight Center
Greenbelt, Maryland

ABSTRACT

A cloud detection algorithm, which utilizes an albedo threshold at 750 nm (α_{750}), was tested on CZCS images of the Southern Ocean. It was found that reducing α_{750} from 1.6% to 0.9% resulted in a marked improvement in cloud detection, masking virtually all of the pixels with negative water-leaving radiances in the ice pack and along the edges of clouds. It was also found that this method was highly sensitive to surface pressure, with a 2% change in pressure resulting in a change of up to 50% in computed pigment concentration, along with a large difference in the number of masked pixels. This method appears to perform well for both low and high reflectance waters, such as in the presence of a large coccolithophore bloom. Manipulating the value of α_{750} allowed masking of those pixels contaminated by sun glint. These results suggest that high latitude scenes previously rejected during the CZCS global processing may be salvaged by applying masks properly.

2.1 INTRODUCTION

CZCS, aboard the NIMBUS-7 satellite, was designed to measure pigment concentrations in the upper ocean using the spectral characteristics of upwelled radiation. Different algorithms have been developed to derive *in situ* pigment concentrations using ratios of measured radiance at 440, 520, and 550 nm (Gordon et al. 1983 and Bricaud and Morel 1987), but these algorithms assume cloud-free skies. It is essential, therefore, that cloud contaminated pixels be masked out before images are processed.

Seawater, and its dissolved and particulate constituents, alter the spectral composition of visible (400–700 nm) radiation reaching the satellite sensor. This is not the case for near-infrared (IR) radiation. Near-IR radiation is strongly absorbed by water, resulting in a uniformly low albedo. Clouds, in contrast, have a wide range of reflectivities at the wavelengths measured by CZCS. Band 5, centered on 750 nm ($\pm$ 50 nm) was the only CZCS band that did not saturate over most clouds and land. Band 5 thus provides the best contrast between clear water and clouds, and is most commonly used in cloud masking algorithms.

Early cloud masking efforts utilized a simple constant threshold method, whereby pixels above a fixed radiance (or number of counts) were excluded as being cloud contaminated. For band 5, this threshold was usually assumed to be 18 counts (Mueller pers. comm.) at low and intermediate latitudes, and 14 counts at higher latitudes. The value of 21 counts was used in the CZCS global processing (Feldman et al. 1989). More sophisticated methods use albedo at 750 nm (α_{750}), calculated as the ratio of upwelled to downwelled radiance, as an indication of the presence of clouds (Eckstein and Simpson 1991). The albedo method is superior to the fixed threshold method because it is able to account for variations in the satellite viewing angle, solar zenith angle, and surface pressure. Empirical observations suggested that pixels with values for α_{750} >1.6% were contaminated by clouds (Eckstein and Simpson 1991 and McClain et al. 1994). Other studies utilized even more complex methods, such as textural analysis and edge detection, to identify the presence of clouds (Gallaudet and Simpson 1991). Darzi (1992) provides an overview of cloud masking algorithms for ocean-viewing sensors.

This paper presents the results of a study intended to assess whether the threshold values reported in Eckstein and Simpson (1991), i.e., α_{750}=1.6%, are applicable to CZCS images of the Southern Ocean. The study also sought to determine whether algorithms designed to identify cloud contaminated pixels could flag pixels influenced by the presence of sea ice.

2.2 METHODS

More than 250 separate CZCS scenes of the Southern Ocean were processed from level-1 to level-2 using a modified version of the SEAPAK program `L2MULT` (McClain

et al. 1991 and McClain and Yeh 1994a). The program L2MULT requires input of the surface pressure, which is then used to calculate the Rayleigh and oxygen optical thicknesses. This modified version of L2MULT is capable of reading surface pressure field files and deriving space- and time-interpolated pressure values for each pixel within a given scene. Ozone data from TOMS is also spatially interpolated to each pixel when TOMS data is available. Scenes may thus be processed assuming that surface pressure and columnar ozone are either spatially constant or variable. L2MULT is also capable of deriving a cloud mask based on either a count threshold for band 5, or the α_{750} threshold. The user may select either method.

The scenes used in this analysis were predominantly of the Ross Sea (November 1978–March 1979, 70° S to 78° S) and the Weddell Sea (March 1986, 72° S to 78° S). Most scenes included land, ice covered waters, open water regions, and cloud covered regions. Solar elevations at the scene centers ranged from 23° to 50°.

The following equation was used to calculate α_{750}:

$$\alpha_{750} = \frac{L_t(750)}{t(750,\theta)\,L_i(750)} \times 100\%, \qquad (10)$$

where $L_t(750)$ is the total radiance at the sensor at 750 nm, $L_i(750)$ is the incident light at 750 nm, $t(750,\theta)$ is the diffuse transmittance between the surface and sensor at 750 nm, and θ is the satellite zenith angle.

The diffuse transmittance between the surface and sensor at 750 nm is calculated as

$$t(750,\theta) = \exp\left[\frac{-(0.5\tau_r + \tau_{oz} + \tau_{ox})}{\cos\theta}\right], \qquad (11)$$

where τ_r, τ_{oz}, and τ_{ox} are the Rayleigh (0.0255), ozone (0), and oxygen (0.02) optical thicknesses, respectively, at 750 nm.

The incident light at 750 nm is computed as

$$L_i(750) = t(750,\theta_0)F_0, \qquad (12)$$

where F_0 is the solar irradiance at 750 nm (mean = 125 mW $cm^{-2}\,\mu m^{-1}\,sr^{-1}$) and θ_0 is the solar zenith angle. The diffuse transmittance between the sun and the ocean surface at 750 nm, $t(750,\theta_0)$, is calculated as

$$t(750,\theta_0) = \exp\left[\frac{-(0.5\tau_r + \tau_{oz} + \tau_{ox})}{\cos\theta_0}\right]. \qquad (13)$$

For the sake of simplicity, much of the analysis presented below focused on a single CZCS scene [orbit number 37118, year 1986, day 60, 16:10:28 Greenwich Mean Time (GMT)] which will be referred to below as scene 1; however, the results were similar for all scenes tested. The results of changes in the α_{750} threshold are also shown for a scene with highly reflective waters containing a rich bloom of coccolithophores (orbit number 8876, year 1980, day 209, 12:29:53 GMT) which will be referred to as scene 2. Another test examined whether changes in the α_{750} threshold would mask pixels affected by sun glint in scene 3 (orbit number 2573, year 1979, day 118, time 9:37:06).

2.3 RESULTS AND DISCUSSION

The following discussion of the results obtained in this analysis addresses five distinct topics. The overall effect of changing the α_{750} threshold value will be examined first. A discussion of the changes that are induced by using variable surface pressure fields, rather than a uniform pressure field, appears in Section 2.3.2. Variations in the constant pressure value used in the analysis also has significant effects, which are discussed in Section 2.3.3. Section 2.3.4 examines the effect of changing the α_{750} threshold on images of high reflectance waters. Section 2.3.5 concerns the use of cloud masking algorithms to flag areas that are affected by sun glint.

2.3.1 Changes in the Albedo Threshold

The frequency histogram of scene 1 (Fig. 1a), processed using an α_{750} threshold of 1.6% (Eckstein and Simpson 1991) and a variable pressure field, revealed an unusual pigment distribution. The unusual feature of this distribution was a pronounced spike at 44 mg m^{-3} (chlorophyll *a* + phaeopigments), i.e., a gray level equal to the maximum value of 254. This spike consisted of 6,983 pixels, which was 10% of the total number of pixels. Most of these pixels were located along the edge of cloud patches and within the sea ice pack (Plate 1†), suggesting that they were contaminated by the presence of clouds or ice, but were not flagged during level-2 processing. Water-leaving radiances for these pixels, at either 520 nm or 550 nm, were negative; consequently, the pigment value for these pixels was set artificially high (equal to a gray level of 254, or a pigment concentration of 46.345 mg m^{-3}). The level-2 processing algorithm in the SEAPAK software used this labeling algorithm as a secondary flagging mechanism. In the case of the 520 nm band, this mechanism was utilized when the water-leaving radiance at 443 nm was less than 0.15 mW $cm^{-2}\,\mu m^{-1}\,sr^{-1}$. Negative water-leaving radiances result when unmasked pixels are contaminated by thin clouds, or are unusually reflective in some other way, i.e., because of sea ice or sun glint. As the calculation of aerosol radiance depends on the assumption of a cloud-free sky, the aerosol radiance is overestimated for these pixels. The resulting calculation of water-leaving radiances at 520 or 550 nm will subsequently yield negative values due to the unusually high aerosol radiances, as water-leaving radiance is calculated by subtracting the aerosol radiance and the Rayleigh radiance from the total radiance.

† All color plates are located in the back of this document.

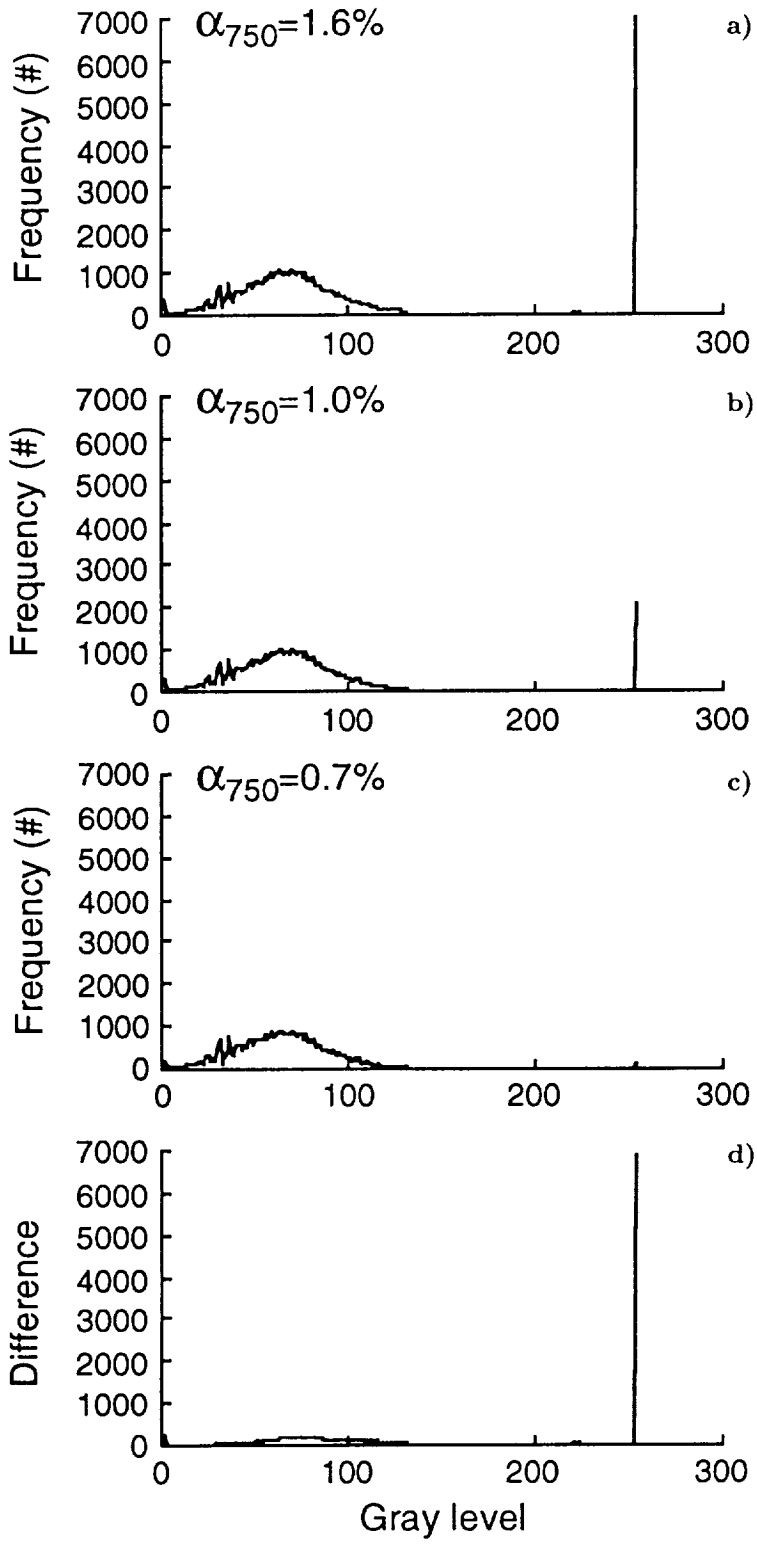

Fig. 1. Gray level frequency distributions for: **a)** the scene where $\alpha_{750} = 1.6\%$ (Plate 1); **b)** the scene where $\alpha_{750} = 1.0\%$; **c)** the scene where $\alpha_{750} = 0.7\%$ (Plate 2); and **d)** the difference between the distributions shown in **a)** and **c)**.

The mean pigment concentration (plus or minus the standard deviation) calculated for scene 1, after applying the cloud mask and removing all pixels with negative water-leaving radiances, was $0.601 \pm 2.596\,mg\,m^{-3}$ (chlorophyll a + phaeopigments). The calculation was based on 59,562 valid pixels (Table 3). Reducing α_{750} to 1.0% lowered the computed pigment concentration to 0.456 ± 1.946 $mg\,m^{-3}$ (chlorophyll a + phaeopigments), with 54,797 valid pixels. Some pixels with negative water-leaving radiances along the cloud and ice edges were still present, however, although the number was reduced substantially, to 2,073 pixels (Fig. 1b). These pixels were not included in the calculation of the mean.

Table 3. Spatially averaged pigment concentrations as a function of albedo threshold for Scene 1. All pigment concentrations have units of $mg\,m^{-3}$.

	Pigment Concentration		
Albedo	*Variable Pressure*	*Constant† Pressure*	*Valid Pixels*
1.6%	0.601 ± 2.596	0.671 ± 2.818	59,462
1.0%	0.456 ± 1.946	0.530 ± 2.254	54,797
0.7%	0.335 ± 1.134	0.406 ± 1.600	48,203

† 1,013.25 mb.

Further reducing α_{750}, to 0.7%, resulted in the masking of virtually all the pixels with negative water-leaving radiances in the ice pack and along the edges of clouds (Plate 2). All except 132 of the pixels with pigment concentrations in excess of $44\,mg\,m^{-3}$ (chlorophyll a + phaeopigments) were masked, leaving most of the previously unmasked pixels intact (Fig. 1c). This value of α_{750} results in a more normal frequency distribution (Fig. 1d). Setting α_{750} reduced the mean pigment concentration for this scene to $0.335 \pm 1.134\,mg\,m^{-3}$ (chlorophyll a + phaeopigments), and reduced the number of valid pixels to 48,203.

2.3.2 Effects of Surface Pressure Fields

The use of a spatially constant standard pressure field of 1,013.25 mb (as used for the CZCS global processing), rather than interpolated pressure fields, resulted in an increase in the computed mean pigment concentration for scene 1. The magnitude of this increase varied as a function of the α_{750} value (Table 3). For example, setting α_{750}=1.6% and holding the pressure constant for the entire scene increased the calculated mean pigment concentration by 12%, from 0.601 to $0.671\,mg\,m^{-3}$ (chlorophyll a + phaeopigments). (The value of $0.601\,mg\,m^{-3}$ was obtained when pressure was allowed to vary spatially.) This difference increased to 21% at α_{750} = 0.7%, which suggests that extra care must be taken in specifying surface pressure at low albedo thresholds.

The choice of schemes used to apply surface pressure to imagery had no impact on the number of pixels masked. However, utilizing a spatially uniform pressure field rather than a spatially variable one resulted in a higher number of pixels with negative water-leaving radiances, which were removed from further analysis. The difference in mean pigment concentration for a given scene, resulting from the choice of either a constant or variable pressure field, was due to changes in pigment concentration for individual pixels only. Differences resulting from this choice were greatest for pixels exhibiting relatively high pigment concentrations (Plate 3).

2.3.3 Surface Pressure Variation

A 2% change in the assigned surface pressure resulted in marked differences in both spatially averaged pigment concentrations and the number of valid pixels for scene 1 (Table 4). The default surface pressure used in the global processing of CZCS imagery (1,013.25 mb) yielded an average pigment concentration of $0.406 \pm 1.600\,mg\,m^{-3}$ from 48,203 valid pixels. A total of 339 pixels had negative water-leaving radiances at 520 or 550 nm, and were assigned a gray level of 254 and excluded. Increasing surface pressure to 1,033.25 mb increased the mean pigment concentration to $0.625 \pm 2.629\,mg\,m^{-3}$, and decreased the number of valid pixels to 47,584. This decrease in valid pixels was due to an increase (to 958) in the number pixels with negative water-leaving radiances at 520 or 550 nm.

Table 4. Spatially averaged pigment concentrations as a function of surface pressure for Scene 1. All pigment concentrations have units of $mg\,m^{-3}$.

Pressure [mb]	*Albedo*	*Pigment Concentration*	*Valid Pixels*
993.25	0.7%	0.306 ± 0.875	48,459
1,013.25	0.7%	0.406 ± 1.600	48,203
1,033.25	0.7%	0.625 ± 2.629	47,584

An increase in pigment concentration at higher pressures is due to the relationship between surface pressure and Rayleigh optical thickness (τ_r). As surface pressure increases, so does τ_r (McClain and Yeh 1994a). Because the 443 nm band is more sensitive to changes in τ_r than the 550 nm band, the 443:550 nm ratio decreases with increasing pressure, resulting in higher pigment estimates. Reducing surface pressure to 993.25 mb lowered the mean pigment concentration to $0.306 \pm 0.875\,mg\,m^{-3}$, and raised the number of valid pixels to 48,459. This decrease in pressure also reduced the number of pixels with negative water-leaving radiances (at 520 or 550 nm) to 83.

2.3.4 High Reflectance Waters

Setting α_{750} to 1.6% in scene 2 (which is a highly reflective image characterized by the presence of a large coccolithophore bloom), resulted in an image containing numerous pixels with negative water-leaving radiances (Plate 4). The low radiance values for these pixels presumably resulted from the presence of thin clouds that were not flagged

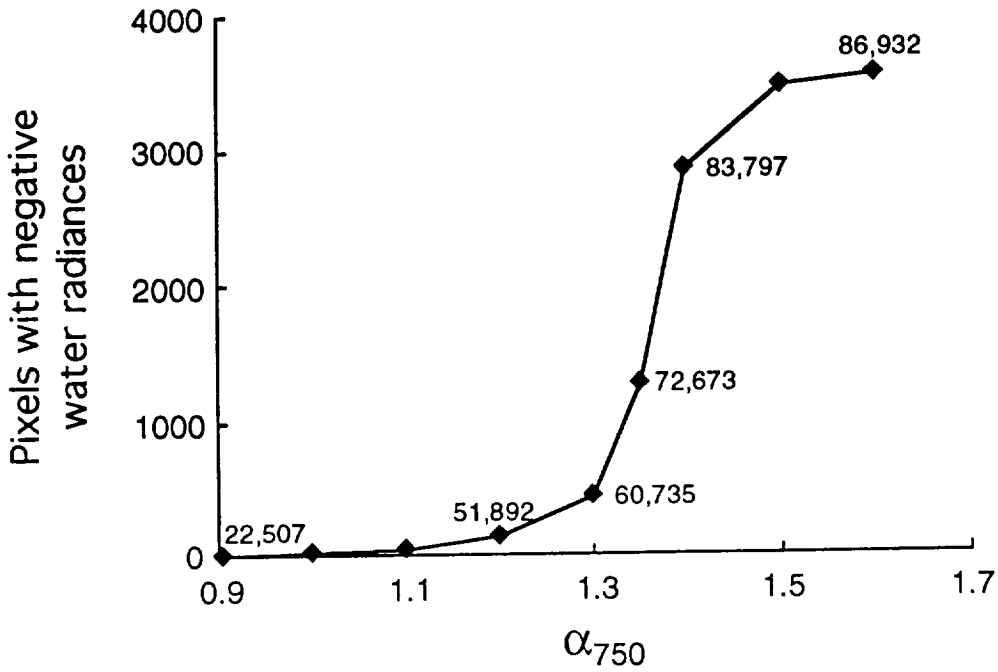

Fig. 2. Variations in the number of pixels having negative water-leaving radiances at 520 or 550 nm as a function of α_{750} (water-leaving radiances at 443 nm were always positive). The numbers associated with each point indicate the number of valid pixels, i.e., pixels with gray levels between 1–253, for each condition.

during routine level-2 processing. Reducing α_{750} from 1.6% to 0.7% masked all pixels with negative water radiances, while retaining more than 80% of the previously valid ones (Plate 5). This observation suggests the use of a reduced α_{750} threshold may even be appropriate for waters that are considered to be highly reflective at visible wavelengths. A refined identification of coccolithophore blooms can be accomplished using other algorithms (Brown 1995).

2.3.5 Sun Glint

Pixels affected by sun glint often have high reflectance values at 750 nm, which may allow them to be flagged with cloud masking algorithms. For example, in scene 3 (McClain and Yeh 1994b), many of the pixels affected by sun glint were masked when $\alpha_{750} = 1.6\%$. The presence of sun glint, however, resulted in numerous pixels with negative water-leaving radiances at 520 and 550 nm, which were not masked when processed with $\alpha_{750} = 1.6\%$. These pixels were located mainly along the edge of the sun glint area masked by the cloud flag, suggesting they were also contaminated. Figure 2 shows that most of the affected pixels can also be masked by reducing α_{750}, e.g., dropping α_{750} from 1.6% to 0.9% masked more than 99% of these pixels. The number of pixels passing the cloud mask, however, was also reduced, from 86,932 to 22,507.

2.4 CONCLUSIONS

These results show that adjusting the albedo threshold can markedly improve image quality. In most scenes, more than 98% of cloud contaminated- and negative water-leaving radiance pixels were removed by reducing α_{750} from 1.6% to 0.7%. Performing similar analyses on more than 250 Southern Ocean scenes suggested that the best value for α_{750} at high latitudes is approximately 0.7–0.9%. Although it is not apparent in the scenes shown, values for α_{750} lower than 0.9%, in general, masked too many valid pixels. The use of α_{750} values higher than 0.9% left too many contaminated pixels unmasked.

Although pixels with negative water-leaving radiances at 520 nm and 550 nm are flagged during level-2 processing, the flag consists of setting the pixel to the maximum pigment concentration so that it can be easily identified. This procedure can lead to problems, however, if the scene contains pixels with genuinely high pigment values that would be indistinguishable from the flagged ones. Masking these pixels with a cloud mask alleviates this problem.

The results presented here also imply that albedo-based cloud masking algorithms are effective at removing pixels contaminated by the presence of sea ice and sun glint. Anomalous pixels located at the pack ice interior, where no obvious cloud cover was present, were eliminated along with the cloud contaminated pixels (compare Plates 1 and 2). This result suggests that many of the scenes from high latitudes, previously rejected in the CZCS global processing quality control program (McClain and Yeh 1994b) because of low solar elevations, may be salvaged by properly applying masks.

Chapter 3

Classification of Coccolithophore Blooms in Ocean Color Imagery

CHRISTOPHER W. BROWN
Goddard Space Flight Center
Greenbelt, Maryland

ABSTRACT

Blooms of the coccolithophore *Emiliania huxleyi*, which occur in the surface layer of the ocean are characterized by high ocean volume reflectance. This high reflectance biases the estimation of satellite-derived geophysical parameters, e.g., pigment concentration, which are based on water-leaving radiance measurements. To avoid erroneous estimates of geophysical parameters in the presence of blooms, it is desirable to implement a simple classification algorithm within the SeaWiFS Data Processing System (SDPS) to flag their occurrence. The development of a supervised, multispectral classification algorithm is described in this chapter. The algorithm groups picture elements (pixels) of the imagery into coccolithophore *bloom* and *non-bloom* classes, based on the normalized water-leaving radiances of each pixel.

3.1 INTRODUCTION

Blooms of the coccolithophore *Emiliania huxleyi*, occurring in the oceanic surface layer, possess a relatively unique high ocean volume reflectance. Because of this optical property, such blooms have been observed in visible satellite imagery from both temperate and subarctic latitudes (Holligan et al. 1983, Balch et al. 1991, Holligan et al. 1993, and Brown and Yoder 1994a and 1994b). The high reflectance, caused principally by the presence of detached coccoliths† (Ackleson and Holligan 1989 and Balch et al. 1991), profoundly affects the optical properties of the surface layer (Aiken et al. 1992 and Holligan et al. 1993). One consequence of this condition is to bias satellite-derived estimates of pigment and chlorophyll *a* concentrations (Gordon et al. 1988b).

One component of the QC process planned for SeaWiFS imagery is to flag the occurrence of coccolithophore blooms, because their presence will affect the accuracy of estimated pigment concentration for that region. A simple classification algorithm has been developed to classify coccolithophore blooms on a global scale in CZCS imagery (Brown and Yoder 1994a). The algorithm, which is suitable to detect the presence of these blooms in the initial processing of SeaWiFS level-1b data, is outlined below. This chapter briefly describes the method followed to establish the decision criteria used in the classification algorithm.

† Coccoliths are microscopic calcareous plates which are produced by living coccolithophores to form a spherical framework called a *coccosphere*. Coccoliths of *E. huxleyi* are shed continuously from the coccosphere during the organism's life cycle.

3.2 METHODS

The classification algorithm is based on the relatively unique spectral signature of coccolithophore blooms, i.e., their high ocean volume reflectance in all of the CZCS visible bands. The algorithm was developed by:

1) Empirically determining the spectral signatures of coccolithophore blooms and various common, non-bloom conditions;
2) Deciding upon feature characters (in this case spectral) to be employed in the algorithm; and
3) Establishing decision boundary values for each of the feature characters that would allow the blooms to be spectrally distinguished from other conditions.

The efficacy of the algorithm in separating the considered conditions was also evaluated. The specific steps involved in image processing, decision criteria development, and algorithm testing are presented below.

3.2.1 Image Processing

Images of normalized water-leaving radiances at three wavelengths [$L_{WN}(440)$; $L_{WN}(520)$; and $L_{WN}(550)$] and

aerosol radiance, $L_a(670)$, from the NASA CZCS data set (Feldman et al. 1989) were rectified to a cylindrical equidistant projection. The imagery had been atmospherically corrected with a multiple scattering atmospheric correction algorithm, using the default maritime aerosol epsilon values (Gordon et al. 1988a). Clouds and sun glint had been masked, and scenes with excessively high aerosol radiance or low sun angles were excluded during initial processing at NASA.

3.2.2 Decision Criteria Development

The spectral signatures of several oceanic conditions—coccolithophore blooms; *clear* blue water; *whitings*, i.e., suspended lime muds (Shinn et al. 1989); sediment-laden water; and unmasked clouds (including cloud *ringing*)—were ascertained by extracting normalized water-leaving and aerosol radiances from pixels located at *training sites* that were centered on portions of level-2 CZCS imagery identified to correspond to each condition (Table 5 and Fig. 3). Most of the training sites were located in the North Atlantic. Those sites representing non-bloom conditions were often selected by contextual, though not necessarily verifiable, evidence. For example, training sites for sediment-laden water were located at, or near, river mouth locations. Sites used to identify whitings came from the Bahamas and the Persian Gulf, areas which are both known for this phenomenon (Robbins and Blackwelder 1992). The eight coccolithophore bloom training sites were positioned in either the *E. huxleyi* bloom sampled by Holligan et al. (1983), or in the high reflectance patches in, and adjacent to, the Gulf of Maine where *E. huxleyi* blooms were sampled in subsequent years (Ackleson and Holligan 1989 and Balch et al. 1991).

The following five feature characters were employed in the classification algorithm:

a) $L_{WN}(440)$;

b) $L_{WN}(550)$;

c) The ratio $L_{WN}(440)/L_{WN}(520)$;

d) The ratio $L_{WN}(440)/L_{WN}(550)$; and

e) The ratio $L_{WN}(520)/L_{WN}(550)$.

The selection of these characters was based, in part, on the suite of characters that proved least redundant in separating the spectral signatures of the various conditions, as determined by examination of the covariance matrix, and also those characters that explained the most variance in stepwise discriminant analysis. The mean and standard deviation for each feature character of the bloom, and for all other spectrally-defined conditions with radiance values less than sensor saturation, i.e., less than 2.55, are presented in Table 6.

Decision boundaries for each of the feature characters (Table 7) were set to values that would exclude the greatest percentage of non-bloom conditions, yet still include the maximum percentage of blooms. An $L_a(670)$ threshold ($1.10\,\mathrm{mW\,cm^{-2}\,\mu m^{-1}sr^{-1}}$), which is slightly greater than twice that of a clear atmosphere (Gordon et al. 1988b), was also set to exclude atmospheric haze. (This threshold is required because the global processing assumed the Ångström exponent was approximately zero, which is typical of marine aerosols, but may not be true near continental boundaries or air masses containing dust.)

The decision boundaries were then incorporated into a non-parametric parallelepiped algorithm that assigned non-land pixels to either the coccolithophore bloom class, or the non-coccolithophore bloom class, by comparing the radiance values of individual pixels to the decision boundaries set for each of the five spectral feature characters. A parallelepiped algorithm classifies an object by comparing the object's features to class (decision) boundaries that form a parallelogram in two-dimensional feature space (Schowengerdt 1983). The algorithm was structured in a manner that was considered to be the most efficient assuming reasonable expectations of the frequency of the various conditions in the oceans (Fig. 4). For example, low reflectance water at $L_{WN}(550)$—representing, presumably, the most common condition in the ocean—was dismissed in the first step.

3.2.3 Algorithm Performance

To evaluate the performance of the decision boundaries in separating the different classes, *test site* pixels (Table 5) were classified, and the percentage of correct and incorrect classifications were calculated based on their previous assignment. As with training site pixels, test site pixels provided a representative spectral signature for each of the various conditions, however, their radiances were not consulted when establishing the decision boundaries.

The effect of the differences in spatial resolution between the training pixels (4 km) and the classified *postage stamp* (PST†) 20 km pixels (Feldman et al. 1989), was assessed using a two-step procedure, in order to evaluate algorithm performance on a global scale. This procedure initially calculated 500 mean radiance values for each condition from 2^n randomly chosen test site pixels (where n ranged from 0–6), and then classified these simulated observations. For these simulations, it was assumed that pixels binned into a PST image represented a random sampling of radiances from a given condition.

3.3 CLASSIFICATION RESULTS

The simulations used to evaluate the efficacy of the classifier revealed that both the number of omissions (i.e., the test bloom pixels excluded during classification from the bloom class) and the number of commissions (i.e., the non-bloom test pixels incorrectly classified into the bloom class), generally decreased as the spatial resolution of the

† PST is a designation for compressed files.

Table 5. Center coordinates and dates for the training and test sites used to establish spectral signatures for coccolithophore bloom and non-coccolithophore bloom conditions. The water conditions or water mass type are designated as follows: *Clear*, clear water; *Coccolithophore*, coccolithophore bloom; *Haze*, aerosol haze; *Sediments*, suspended sediments; *Red*, *red* water condition; and *Whitings*, whitings. Latitude and longitude are in decimal degrees. For the date field, YY is the decadal year and DDD is the sequential day of the year.

Date YY DDD	*Water Condition*	*Training Site*			*Testing Site*		
		Latitude	*Longitude*	*Code*	*Latitude*	*Longitude*	*Code*
83 153	Clear	39.54°N	70.81°W	[3]	38.48°N	71.05°W	[3]
83 180	Clear	43.49°N	66.43°W	[1]	46.59°N	58.72°W	[2]
83 181	Clear	42.75°N	63.96°W	[2]	42.48°N	62.05°W	[2]
83 182	Clear	43.49°N	60.13°W	[2]	42.48°N	62.05°W	[2]
83 191	Clear	41.03°N	64.24°W	[2]	40.52°N	65.10°W	[3]
79 188	Coccolithophore	42.40°N	64.28°W	[2]	42.55°N	63.69°W	[2]
82 147	Coccolithophore	48.25°N	8.45°W	[5]	48.13°N	6.85°W	[5]
82 148	Coccolithophore	48.25°N	8.45°W	[5]	48.13°N	6.85°W	[5]
82 149	Coccolithophore	48.29°N	8.53°W	[5]	48.13°N	6.92°W	[5]
83 153	Coccolithophore	42.24°N	68.93°W	[1]	41.54°N	68.39°W	[1]
83 160	Coccolithophore	42.59°N	69.13°W	[1]	43.14°N	69.44°W	[1]
83 180	Coccolithophore				43.14°N	69.29°W	[1]
	Coccolithophore				42.75°N	68.29°W	[1]
83 181	Coccolithophore	42.44°N	69.01°W	[1]	42.36°N	67.84°W	[1]
	Coccolithophore				41.89°N	69.05°W	[1]
	Coccolithophore				42.63°N	67.33°W	[1]
83 182	Coccolithophore	42.01°N	68.93°W	[1]	42.16°N	68.15°W	[1]
	Coccolithophore				42.52°N	68.35°W	[1]
83 194	Haze	42.16°N	69.25°W	[1]	43.61°N	63.65°W	[2]
83 210	Haze	41.61°N	69.25°W	[3]	40.71°N	70.19°W	[3]
85 247	Red	39.07°N	73.63°W	[3]	39.58°N	73.75°W	[3]
79 125	Sediments	6.24°N	53.85°W	[6]	5.81°N	53.50°W	[6]
79 164	Sediments	1.94°N	48.69°W	[6]	5.81°N	53.03°W	[6]
79 177	Sediments	48.54°N	68.70°W	[4]	47.76°N	69.76°W	[4]
79 185	Sediments				47.76°N	69.76°W	[4]
79 202	Sediments	5.58°N	52.68°W	[6]	5.89°N	53.58°W	[6]
	Sediments				5.66°N	52.91°W	[6]
79 208	Sediments	5.77°N	53.30°W	[6]	6.20°N	56.24°W	[6]
	Sediments	0.22°S	47.82°W	[6]	5.97°N	53.54°W	[6]
79 208	Sediments	6.01°N	56.16°W	[6]	5.03°N	52.09°W	[6]
85 273	Sediments	41.11°N	70.62°W	[3]	41.22°N	71.05°W	[6]
79 004	Whitings	28.15°N	50.82°E	[7]	27.89°N	49.27°E	[7]
79 015	Whitings	27.78°N	50.68°E	[7]	24.51°N	53.95°E	[7]
79 028	Whitings	28.09°N	50.05°E	[7]	26.39°N	50.78°E	[7]
79 032	Whitings	28.95°N	50.21°E	[7]	26.39°N	50.78°E	[7]
80 023	Whitings	21.15°N	71.67°W	[8]			
80 024	Whitings				21.15°N	71.67°W	[8]

[1] Gulf of Maine, western North Atlantic.
[2] Nova Scotia Shelf or Slope, western North Atlantic.
[3] New York Bight or Slope Water off the northeastern US, western North Atlantic.
[4] St. Lawrence River, western North Atlantic.
[5] Celtic Shelf, eastern North Atlantic.
[6] Coastal waters of northeastern South America, equatorial North Atlantic.
[7] Persian Gulf.
[8] Bahamas, equatorial North Atlantic.

Table 6. Spectral statistics (mean ± standard deviation) from training sites of the environmental conditions when CZCS band 3 (550 nm) was not saturated. The water types are designated by the following codes: *Clear*, clear water; *Coccolithophore*, coccolithophore bloom; *Haze*, atmospheric haze; *Red*, *red* water condition; *Sediments* sediments; *Outflow*, river outflow; and *Whitings*, whitings. $L_{WN}(\lambda)$ represents the normalized water-leaving radiance, with units of $\mathrm{mW\,cm^{-1}\,\mu m^{-1}\,sr^{-1}}$ (from Brown and Yoder 1994a).

Water Condition	*Number of Images*	$L_{WN}(440)$	$L_{WN}(550)$	$L_{WN}(440)/L_{WN}(520)$	$L_{WN}(440)/L_{WN}(550)$	$L_{WN}(520)/L_{WN}(550)$
Clear	1,435	0.80 ± 0.20	0.42 ± 0.87	1.4 ± 0.30	2.0 ± 0.50	1.4 ± 0.19
Coccolithophore	1,095	1.92 ± 0.41	1.43 ± 0.42	1.1 ± 0.14	1.4 ± 0.27	1.3 ± 0.11
Haze	360	1.95 ± 0.44	0.99 ± 0.07	1.5 ± 0.29	2.0 ± 0.43	1.3 ± 0.07
Red	180	1.08 ± 0.15	1.24 ± 0.08	1.0 ± 0.11	0.9 ± 0.13	0.9 ± 0.06
Sediments	1,189	1.17 ± 0.48	1.92 ± 0.39	0.6 ± 0.20	0.6 ± 0.27	1.0 ± 0.15
Outflow	136	0.40 ± 0.26	0.82 ± 0.19	0.5 ± 0.16	0.5 ± 0.41	1.1 ± 0.61
Whitings	838	2.06 ± 0.35	1.40 ± 0.43	1.2 ± 0.33	1.6 ± 0.67	1.3 ± 0.14

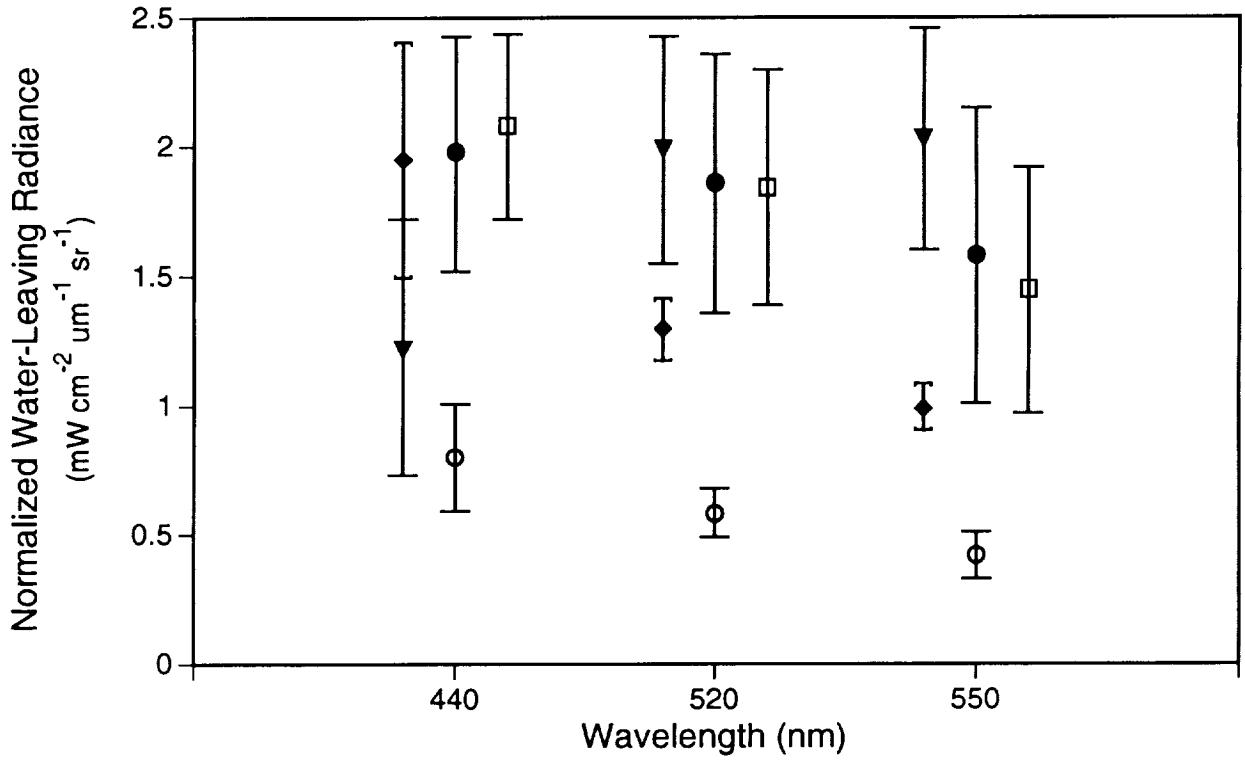

Fig. 3. Mean (x + standard deviation) normalized water-leaving radiances for coccolithophore blooms (•), *clear* blue water (○), haze (♦), sediments (▼), and whitings (□) at the band wavelengths of the CZCS (from Brown and Yoder 1994a).

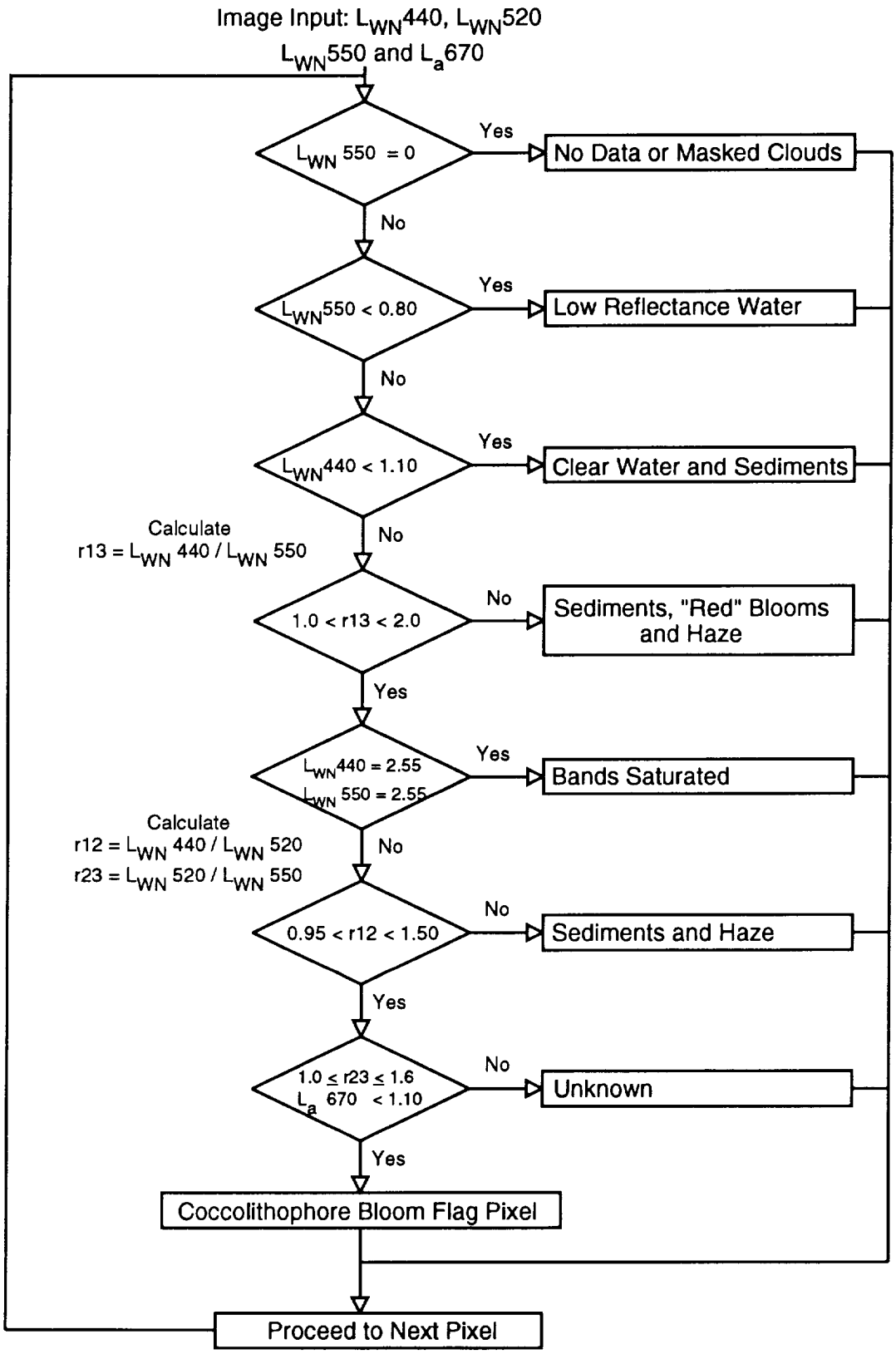

Fig. 4. Flow diagram illustrating the coccolithophore bloom detection algorithm developed for use with CZCS global processing data products.

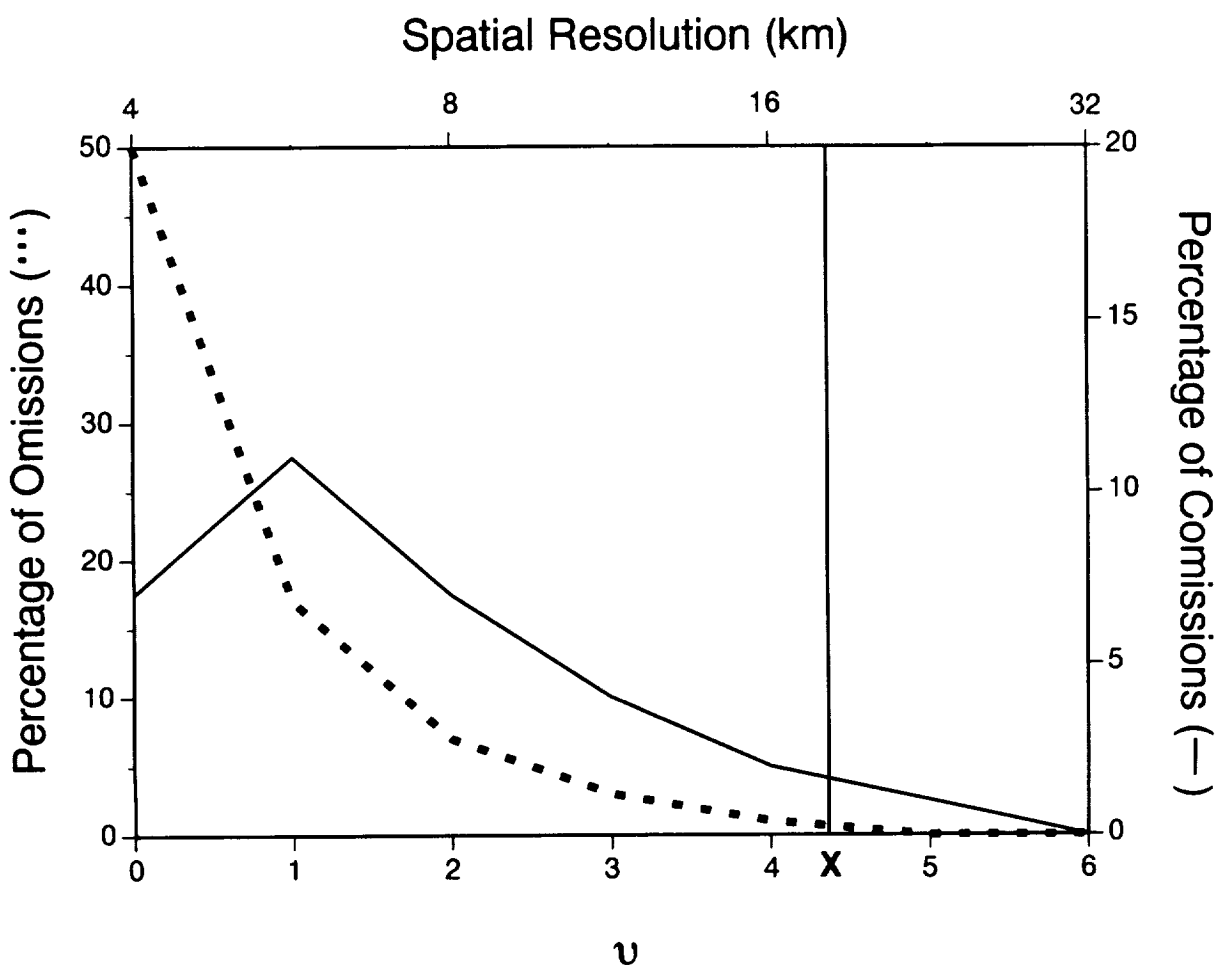

Fig. 5. An evaluation of classification performance at different spatial resolutions. The spectral signatures of bloom and non-bloom conditions at different pixel spatial resolutions were simulated by increasing the sample size (n is equal to 2^n) of pixels used to compute the mean radiance value of a single PST pixel. The mean number of level-2b pixels comprising all valid PST pixels in this study, i.e., 18, is denoted by the vertical line at **X**. Omissions indicate the percentage of test bloom pixels excluded from the bloom class after classification and commissions indicated the percentage of non-bloom pixels incorrectly included in the classified bloom class. These results do not include the testing of whitings (Brown and Yoder 1994a).

imagery decreased (Fig. 5). The combined percentage of commissions and omissions decreased to less than 3% when the simulated sample size (2^n) was 16, equivalent to a spatial resolution of 16 km^2 (Fig. 5). Note that an average of 18 level-2 pixels (out of a nominal maximum of 25) were binned to compute the mean radiance of a single 5-day PST pixel (Brown and Yoder 1994a). These simulation results suggest, therefore, that most pixels are accurately classified at this low spatial resolution. At higher spatial resolutions, however, the percentage of omissions and commissions increases. This finding reveals that the algorithm is not accurate for higher resolution CZCS imagery, i.e., level-2, in regions where conditions with spectral signatures, which mimic coccolithophore blooms, exist.

Whitings, sediment, and atmospheric haze were the only non-bloom conditions misclassified as blooms during the testing simulations. Whitings were spectrally indistinguishable from coccolithophore blooms using the present classification scheme. Caution must be taken, therefore, when assigning the cause of a flagged pixel, particularly at lower latitudes where these conditions are most predominant.

Examples of the results from the detection algorithm are illustrated in Plate 6. The top left and top right images in Plate 6 are true-color composites of CZCS images that show coccolithophore blooms located in the North Atlantic Ocean south of Iceland, and on the northeastern US continental shelf, respectively. The image of the Icelandic bloom (orbit 8876) was processed using the default atmos-

pheric correction epsilon coefficients. The image of the US continental shelf (orbit 3171), which is also presented in Gordon et al. (1983), was processed manually to remove a significant aerosol signal (Ångström exponent = 0.6). The blooms appear milky white to turquoise in color, and clouds are masked black.

The coccolithophore flag masks of these images (Plate 6, bottom left and bottom right) reveal the effectiveness of the algorithm in both the open ocean and the more complex coastal environment. Coccolithophore blooms are colored white and non-bloom conditions are colored blue. Note in the top right image that the relatively high reflectant yellow waters located just south of Cape Cod (the prominent U-shaped peninsula) were not grouped into the bloom class (bottom right).

Table 7. Decision boundary values of the feature characters used at the global and regional scale. Radiance values are given in units of $\mathrm{mW\,cm^{-1}\,\mu m^{-1}\,sr^{-1}}$.

Feature Character	*Global Value*
$L_{WN}(440)$	$1.10 < x < 2.55$
$L_{WN}(550)$	$0.80 \leq x < 2.55$
$\frac{L_{WN}(440)}{L_{WN}(520)}$	$0.95 \leq x \leq 1.50$
$\frac{L_{WN}(440)}{L_{WN}(550)}$	$1.00 < x < 2.00$
$\frac{L_{WN}(520)}{L_{WN}(550)}$	$1.00 \leq x \leq 1.60$

The results of the algorithm indicate that its performance is quite good in the higher latitudes, based on comparisons with what was previously known of the distribution pattern of coccolithophore blooms and other potentially mimicking conditions (Brown and Yoder 1994a). At the lower latitudes, however, discrimination of high reflectance signals, caused by coccolithophore blooms from other sources of high reflectance, will likely remain problematic.

3.4 DISCUSSION

The detection of coccolithophore blooms is sensitive to light backscattered from approximately one attenuation depth in the water column, and is primarily a function of coccolith, not cell, concentration (Balch et al. 1991). The detection of coccolithophore blooms occurring in the surface layer is consequently biased toward the declining stage, i.e., *stationary phase*, of the bloom, when the proportion of coccolith-to-cell concentration is greatest (Balch et al. 1991). It is presumed that all patches recognized as blooms are composed of the coccolithophore *E. huxleyi*, the only species presently documented to be visible in satellite imagery (Balch et al. 1991 and Holligan and Balch 1991).

The coccolithophore bloom detection algorithm described above is a simple and intuitive approach based on the empirically derived spectral signatures of coccolithophore bloom and non-bloom conditions. The ability of the algorithm to detect blooms will most likely improve when used with SeaWIFS imagery, due to the planned improvement in atmospheric correction and cloud masking procedures.

ACKNOWLEDGMENTS

Drs. E-n. Yeh and C.R. McClain provided the processed CZCS images and commented on the text.

Chapter 4

A Proposed On-Orbit, Out-of-Band Correction Scheme for SeaWiFS

ROBERT A. BARNES
ManTech Environmental Technology, Inc.
Wallops Island, Virginia

WAYNE E. ESAIAS
CHARLES R. MCCLAIN
Goddard Space Flight Center
Greenbelt, Maryland

ABSTRACT

Out-of-band responses for the eight SeaWiFS bands are elements of the instrument's radiometric calibration. In that calibration, the instrument views a broad area of known radiance, and the output from the bands are recorded in counts. The counts from each band include the out-of-band contribution, and these out-of-band contributions are functions of the spectral shape of the source that is measured. The SeaWiFS laboratory calibration, therefore, has the out-of-band correction for a 2,850 K source factored into its results. If the instrument measures a source with that particular spectral shape, those measurements automatically contain appropriate out-of-band corrections. The prelaunch calibration equations for SeaWiFS contain correction terms that convert the out-of-band responses from those for a 2,850 K source to those for a 5,900 K source. As a result, the SeaWiFS calibration equations now have the out-of-band correction for a 5,900 K source factored into them. The 5,900 K spectral shape closely duplicates the spectral shape for SeaWiFS ocean measurements. The errors arising from the use of the 5,900 K out-of-band corrections for ocean measurements are estimated to be small, on the order of a few tenths of a percent. If an alternate out-of-band correction is to be used, then the 5,900 K correction must be removed from the measurement results and a new out-of-band correction inserted in its place. An out-of-band correction based on the actual measurements from SeaWiFS, plus the procedure for its implementation, is presented here.

4.1 SPECIFICATION

The specifications of the Ocean Color Data Mission (OCDM) contract call for an out-of-band response that is less than 5% of the within-band value (Barnes et al. 1994a). For this specification, within-band is defined as the wavelength interval between the upper and lower 1% response points. The within-band response is the integrated instrument response between these points. Out-of-band includes everything else, both above and below the 1% response points. The 1% response points are also called the upper and lower extended band edges. The wavelengths for these edges can be found in Table 13 of Barnes et al. (1994b), which is reproduced as Table A-1 in Appendix A of this document.

The specifications call for the out-of-band response to be determined for a radiant source with a spectral shape equivalent to the sun. For practical purposes, including out-of-band calculations, the sun can be considered as a 5,900 K blackbody (Allen 1973 and Warneck 1988).

Figure 6 shows the spectral shape of two blackbodies (5,900 K and 2,850 K). One has the spectral shape of the solar output and the other the spectral shape of the light source used in the laboratory. These blackbody curves have been normalized to the typical input radiance for SeaWiFS band 1, as given in the performance specifications. For a 5,900 K source, an out-of-band response, i.e., a light leak, near 500 nm will be emphasized, relative to a leak near 1000 nm. For a 2,850 K source, however, the reverse is true. The out-of-band portion of a SeaWiFS measurement, therefore, includes more than the wavelength-dependent response of the instrument—it also includes the wavelength-dependent shape of the radiance measured by the instrument.

To facilitate out-of-band calculations, the response of the instrument (called the *system response*) to a *spectrally*

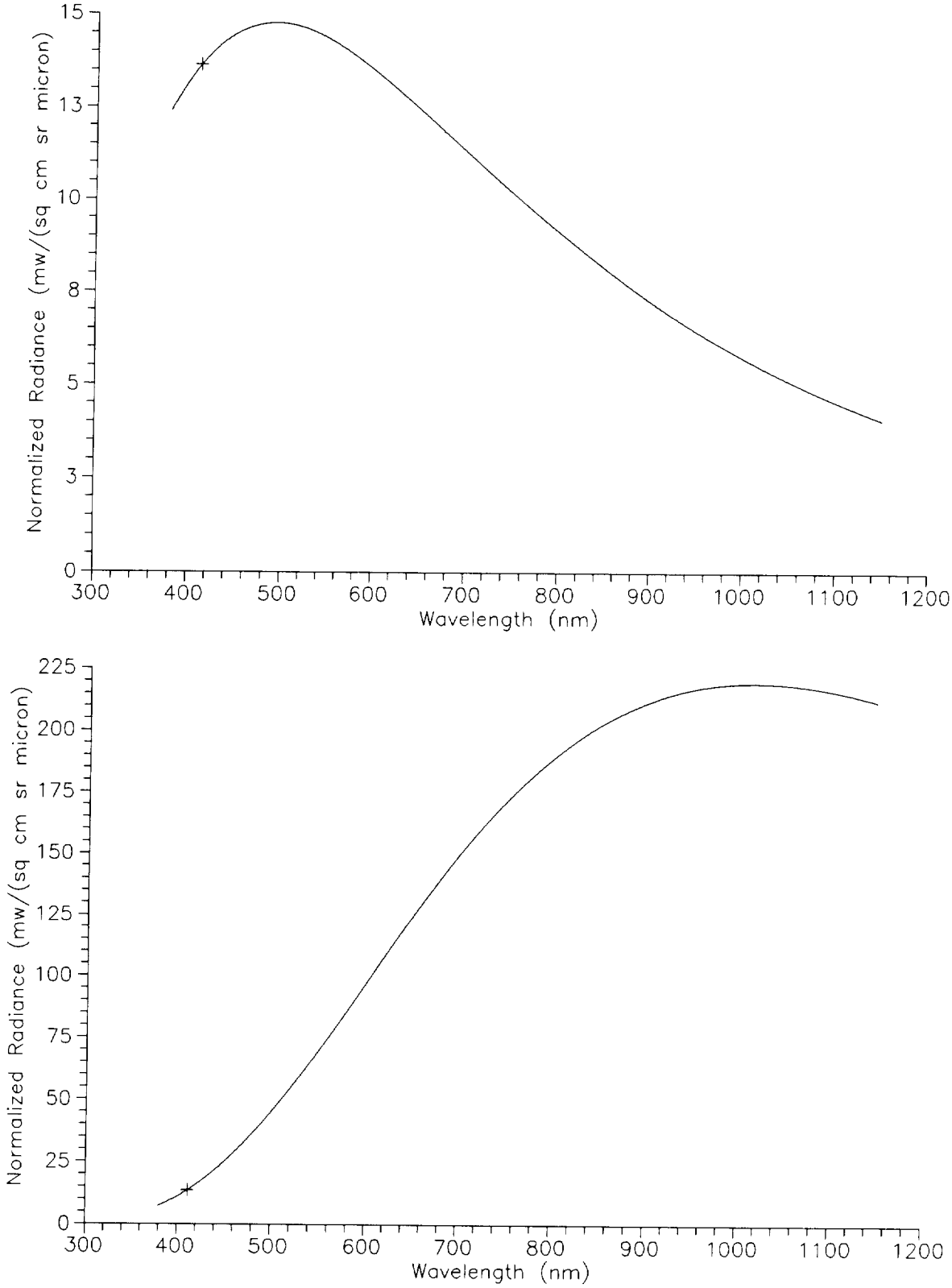

Fig. 6. Blackbody radiance curves normalized to the typical radiance at 412 nm from the SeaWiFS specification. The top panel shows the curve for a 5,900 K blackbody that approximates the solar spectrum. The bottom panel shows the curve for a 2,850 K blackbody that approximates the SBRC integrating sphere.

flat light source, i.e., to a light source with a radiance of $1\,mW\,cm^{-2}\mu m^{-1}sr^{-1}$, was calculated at each wavelength from 380–1,150 nm. Barnes et al. (1994b) details the development of this response calculation. Figure 7 shows this system response curve for SeaWiFS band 1. This response has been calculated from measurements of the transmittances and reflectances of the optical components for the band, and from the response of the photodiode. The output for the band in Fig. 7 is given as nanoamperes (nA) from the photodiode at each 1 nm interval for the measurements of the spectrally flat source.

The radiance sources in Fig. 6 are given as mW of radiance at each 1 nm interval. It is a straightforward calculation to multiply the instrument response and the radiance at each 1 nm interval to give the response of the instrument to the radiant source. Such calculations were made for the response of each SeaWiFS band to a 5,900 K blackbody source in Table 14 of Barnes et al. (1994b), (reproduced as Table A-2 in Appendix A). The calculations in that table include the integrated values for the lower out-of-band response (from 380 nm to the lower extended band edge), for the in-band response (from the lower to the upper extended band edge), and for the upper out-of-band response (from the upper extended band edge to 1,150 nm). The percent out-of-band response is calculated as the sum of the individual out-of-band responses divided by the in-band response. It is important to note that in these calculations the absolute values for the light intensity from the radiant source are not important. It is the wavelength-dependent shape (in relative terms) for the source that is important. The percent out-of-band response is calculated as a ratio.

4.2 OUT-OF-BAND CORRECTION

The percent out-of-band responses in Table A-2 are given for a source with a 5,900 K blackbody shape. This source approximates the spectral shape for the output of the sun. SeaWiFS, however, will measure upwelling radiances from the Earth, radiances with a spectral shape different from that for the sun. It is proposed here that the on-orbit SeaWiFS measurements can be used to provide the spectral shape for the radiant source in the out-of-band calculations.

Figure 8 gives the typical input radiances for the eight SeaWiFS bands. These radiances have been taken from the specifications for the instrument. The radiances have been connected by lines such that the radiances at the intervening wavelengths can be calculated by linear interpolation. The radiance at 380 nm has been arbitrarily made the same as that for SeaWiFS band 1 at 412 nm. In the same manner, the radiance value at 1,150 nm has been set to one-third of the radiance value for SeaWiFS band 8 at 865 nm. Such extensions must be introduced since the SeaWiFS bands do not completely cover the wavelength range from 380–1,150 nm.

There are significant reasons behind the selection of the end-point values given above. In Fig. 9, the typical SeaWiFS radiances have been plotted against three blackbody curves: 10,000 K, 12,000 K, and 14,000 K. These curves are hotter, and therefore *bluer*, than the 5,900 K solar spectrum. The three curves have each been normalized to give the typical radiance value for SeaWiFS band 1 at 412 nm. The typical SeaWiFS radiances in Fig. 9 approximate the spectral shape of blue light upwelling from the atmosphere, that is, of light dominated by Rayleigh scattering. For most SeaWiFS ocean measurements, the upwelling radiance from the Earth is dominated by the atmosphere.

In Fig. 9, the radiance from the three curves is greater at 380 nm than at 412 nm. For the 5,900 K blackbody curve in Fig. 6, the value at 380 nm is less than that at 412 nm. It seemed appropriate to split this difference and to set the 380 nm value in the on-orbit radiance spectrum equal to that at 412 nm. This setting represents an extrapolation of about 15 nm in the reference spectrum, since the lower extended band edge for SeaWiFS band 1 is located at about 395 nm.

For the upper end of the reference spectrum, 1,150 nm, the extrapolation is about 240 nm, since the upper extended band edge for SeaWiFS band 8 is at about 910 nm. In this case, however, the four reference curves (the three curves in Fig. 9 and the 5,900 K curve in Fig. 6) all give values at 1,150 nm that are significantly lower than the value at 865 nm. From the curves in Fig. 9, it was determined that a reduction in radiance from 865–1,150 nm by a factor of three seemed appropriate.

4.3 IMPLEMENTATION

For a SeaWiFS pixel of Earth-exiting radiance, it is possible to calculate a set of radiances from 380–1,150 nm as presented above. Using the spectrally flat instrument response spectra from Section 4.1, it is possible to perform a point-by-point multiplication to obtain the output at each wavelength from 380–1,150 nm. Using the lower and upper extended band edges in Table A-2, the percent out-of-band response for the Earth-exiting radiance can be calculated. The fractional out-of-band response for a 5,900 K blackbody (see Table A-2) can be removed from the measurements, and the fractional correction for the Earth-exiting radiance can be applied in its place.

As this procedure is developed by the researcher, it is important to bear in mind that the out-of-band response is an integral part of the laboratory calibration of the instrument. The out-of-band counts from the instrument are part of the total counts that SeaWiFS produces when exposed to the laboratory radiance source. Earth-exiting radiance will generate a different number of counts from the out-of-band portion of the spectrum. This difference in counts must be reassessed from pixel to pixel if the measurements are to be made with the greatest accuracy.

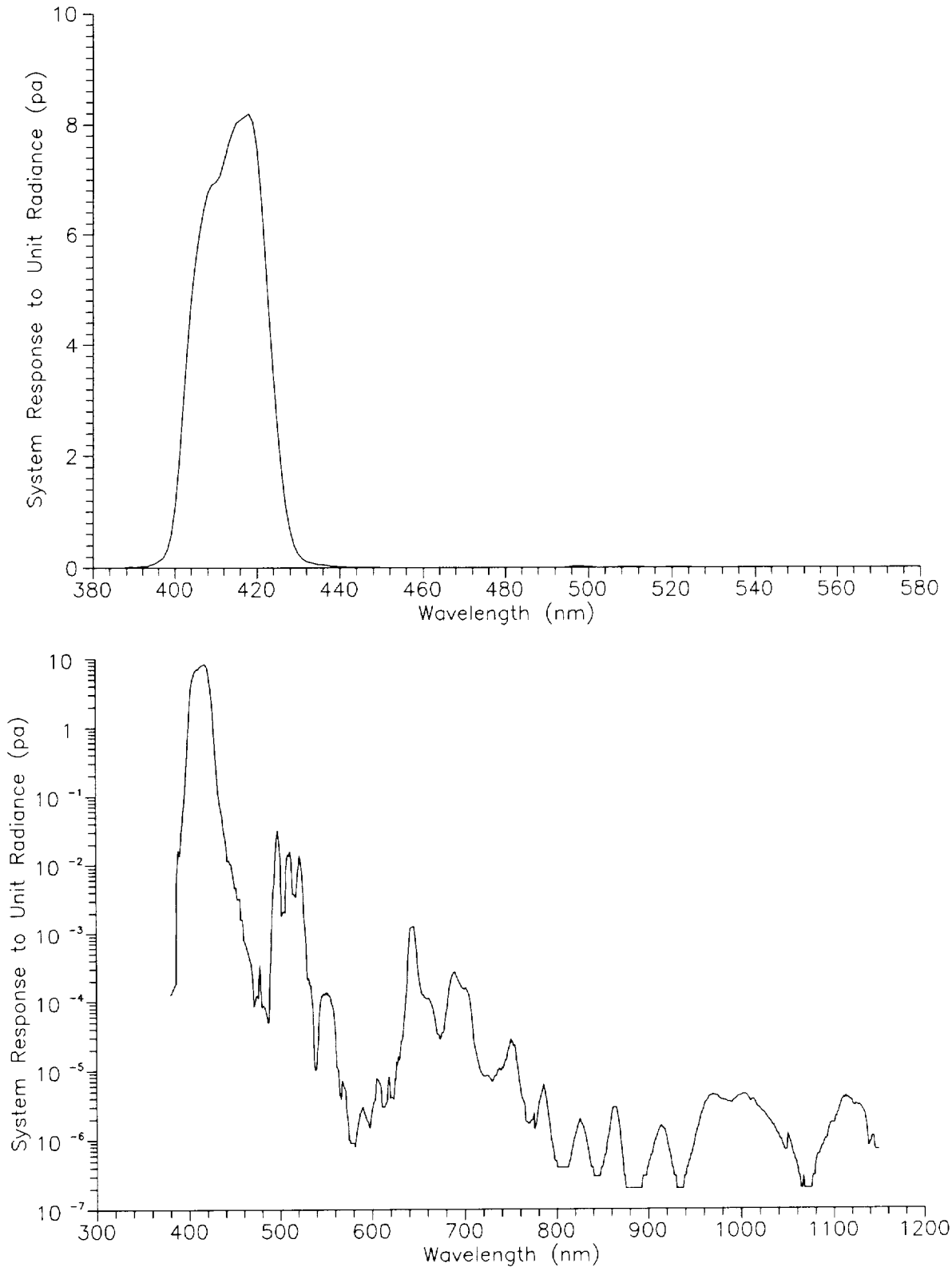

Fig. 7. System response curve for SeaWiFS band 1. This data includes the optical components and the photodiode response to a spectrally flat light source with a radiance of 1 mW cm^{-2} sr^{-1} μm^{-1}. The top panel shows the system response on a linear scale. The out-of-band response near 500 nm is barely noticeable. The bottom panel illustrates the system response on a logarithmic scale.

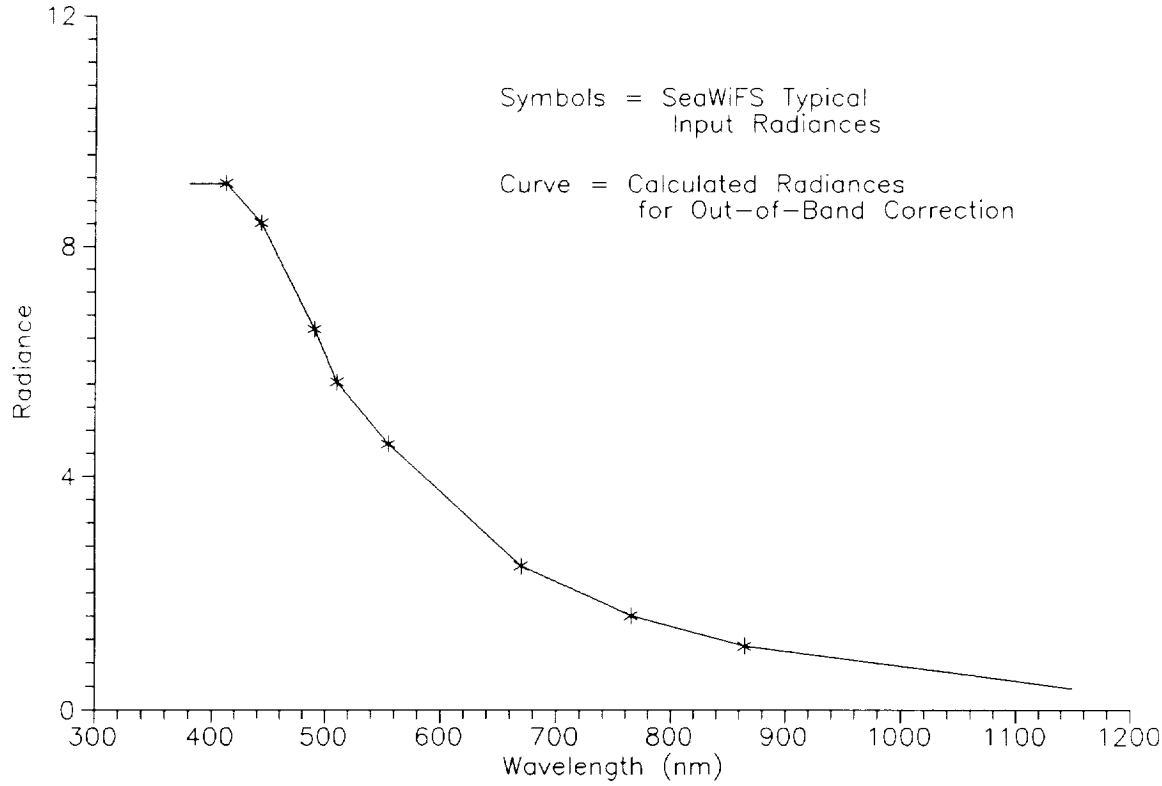

Fig. 8. A spectrum of upwelling Earth radiance based on the SeaWiFS typical input radiances. Radiance curves of this type, using actual SeaWiFS measurements, are proposed for the on-orbit out-of-band correction calculations.

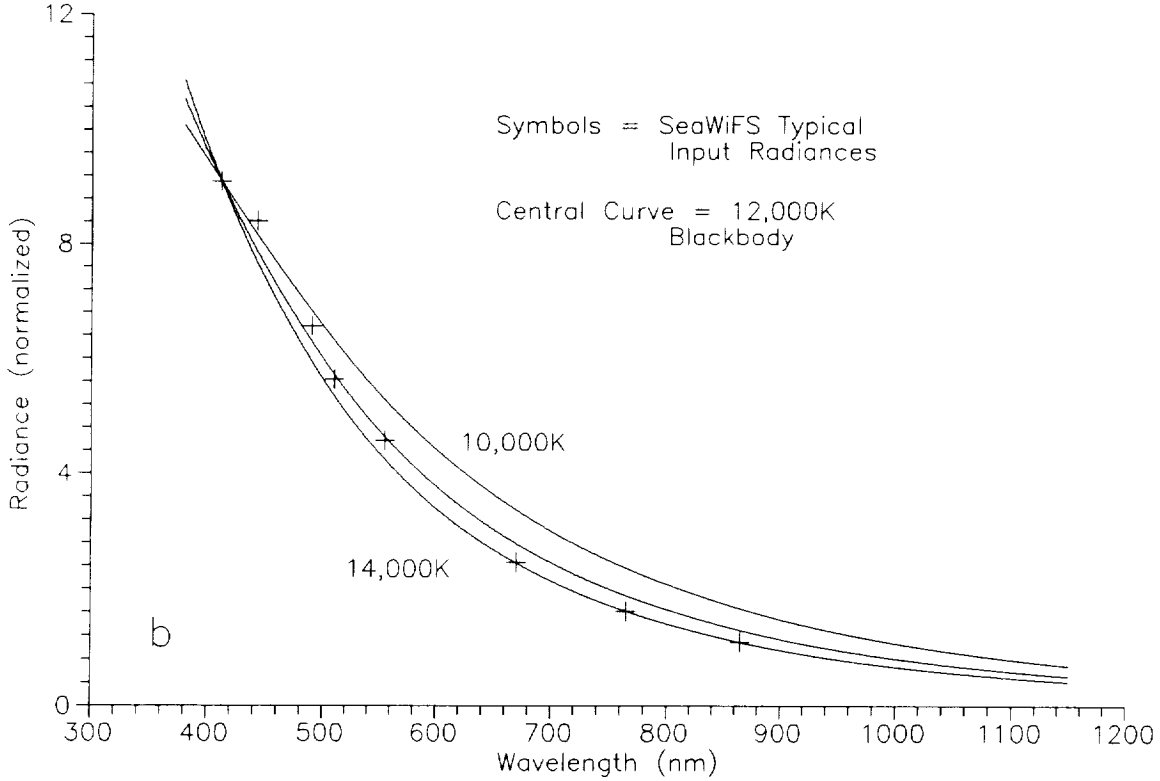

Fig. 9. Typical input radiances from SeaWiFS are plotted with three blackbody radiance curves. The high temperatures of the radiance curves indicate a radiance source that is more *blue* than the sun, i.e., the sources have more emission in the blue portion of the visible spectrum.

There is a second technique for converting the out-of-band contribution to the laboratory calibration. This involves the calculation of the sum over the wavelength range from 380–1,150 nm for each band and for each source's spectral shape (Barnes et al. 1994b). The correction can be applied using the ratios of these integrals. There is a normalization process required in this second method, however, since the integral values for the 2,850 K and 5,900 K results have been calculated using the saturation radiance for each band at its nominal center wavelength. These values are given in Table 11 of Barnes et al. 1994a. These radiances are:

a) 13.63 mW, at 412 nm, for band 1;

b) 13.25 mW, at 443 nm, for band 2;

c) 10.50 mW, at 490 nm, for band 3;

d) 9.08 mW, at 510 nm, for band 4;

e) 7.44 mW, at 555 nm, for band 5;

f) 4.20 mW, at 670 nm, for band 6;

g) 3.00 mW, at 765 nm, for band 7; and

h) 2.13 mW, at 865 nm, for band 8.

The normalization procedure for the integrals is necessary because the Earth-exiting radiance measured for each band on orbit will not have the corresponding value listed above at the band's central wavelength.

4.4 CONCLUDING REMARKS

As shown in Table A-1, the out-of-band responses for the eight SeaWiFS bands range from about 0.3% to about 3.7%. These responses were calculated for a 5,900 K blackbody source, a source that duplicates the solar spectrum. The 5,900 K source approximates the spectral shape of the upwelling Earth radiance for SeaWiFS ocean measurements. The actual measurements made by SeaWiFS on orbit will, however, give an improved spectral shape for the upwelling radiance. The authors have proposed to use the actual measurements at the eight SeaWiFS bands (412, 443, 490, 510, 555, 670, 765, and 865 nm) plus two calculated values (at 380 and 1,150 nm) to form the radiance spectrum for the out-of-band calculation. The value at 380 nm is set equal to that at 412 nm, and the value at 1,150 nm is set to one-third the value at 865 nm.

Although an extensive error analysis has not been performed, it is thought that an out-of-band correction using this instrument-based spectrum should provide a calculated out-of-band amount that is good to within a few tenths of a percent.

4.5 DATA ACCESS

Files that contain the response of the SeaWiFS bands are available from GSFC. There are three American Standard Code for Information Interchange (ASCII) files. The first, `SPECREAD.ME`, gives an explanation of the two files that contain the spectral response data. The second, `SPECTRA1.DAT`, gives the response values for SeaWiFS bands 1–4. The third file, `SPECTRA2.DAT`, gives the response values for SeaWiFS bands 5–8. It is currently possible to obtain the information through the Goddard Distributed Active Archive Center (DAAC). For further information about access to the DAAC data, contact:

DAAC/User Services Office
NASA/GSFC/Code 902.2
Greenbelt, MD 20771
Voice: 301–286–3209
Fax: 301–286–1775
Net: `daacuso@daac.gsfc.nasa.gov`

Chapter 5

Algorithm for the Application of the Sensor Calibration for SeaWiFS Level-2 Processing

MICHAEL DARZI
FREDERICK S. PATT
General Sciences Corporation
Laurel, Maryland

LAKSHMI KUMAR
Hughes STX
Lanham, Maryland

ABSTRACT

The processing of SeaWiFS level-1 data to level-2 requires that the sensor calibration be applied to the raw counts, prior to the derivation of geophysical values. The algorithm described herein is the implementation of the sensor calibration approach of Barnes et al. (1994b). The algorithm is designed for operational use by the SeaWiFS Project, and works on individual scan lines of SeaWiFS level-1a data, returning sensor-calibrated radiance values (level-1b data). Calibration data used in the calculations are stored in the *sensor calibration table*, which is also described.

5.1 INTRODUCTION

This document describes the algorithms of two SeaWiFS operational routines, `calibrate_l1a` and `get_cal`. These routines are used to apply the sensor calibration to level-1a data during the generation of level-2 products (Fig. 10). The algorithms implement the sensor calibration approach described in Barnes et al. (1994b). The calibration data are stored in the sensor calibration table, which is also described in this document.

5.2 THE `calibrate_l1a` ALGORITHM

The processing of level-1 data to level-2 requires that the sensor calibration be applied to the raw counts, prior to the derivation of geophysical values. The level-1a data calibration routine, `calibrate_l1a`, takes an array of raw counts (level-1a data) and, after applying the sensor calibration, returns a corresponding array of radiance values (level-1b data). It is designed to work on part, or all, of a scan line at a time. The interface specifications for this routine are given in an interface specifications document written for the SeaWiFS Project and authored by M. Darzi.

5.2.1 Variables

The following subsections define the variables used in the pseudocode of the `calibrate_l1a` algorithm (5.2.2).

5.2.1.1 Input Arguments

The following variables provide data required by `calibrate_l1a` and, therefore, comprise its input arguments as passed by the level-2 processing program:

- `cal_path` (character): the directory path and filename for the sensor calibration table file (used by `get_cal`);
- `syear` (2-byte integer): the year of the scene start time (used by `get_cal`);
- `sday` (2-byte integer): the day of the year for the scene start time (used by `get_cal`);
- `smsec` (4-byte real): the milliseconds of the day for the scene start time (used by `get_cal`).
- `eday` (2-byte integer): the day of the year for the scene end time (used by `get_cal`);
- `msec` (4-byte real): the scan line time in milliseconds of the day (used by `get_cal`);
- `dtype` (character): the data type flag (used by `get_cal`);
- `st_samp` (4-byte integer): the number (one-relative, i.e., relative to an initial value of one) of the first sample to process on each scan line;
- `nsamp` (4-byte integer): the number of samples to process in each scan line;

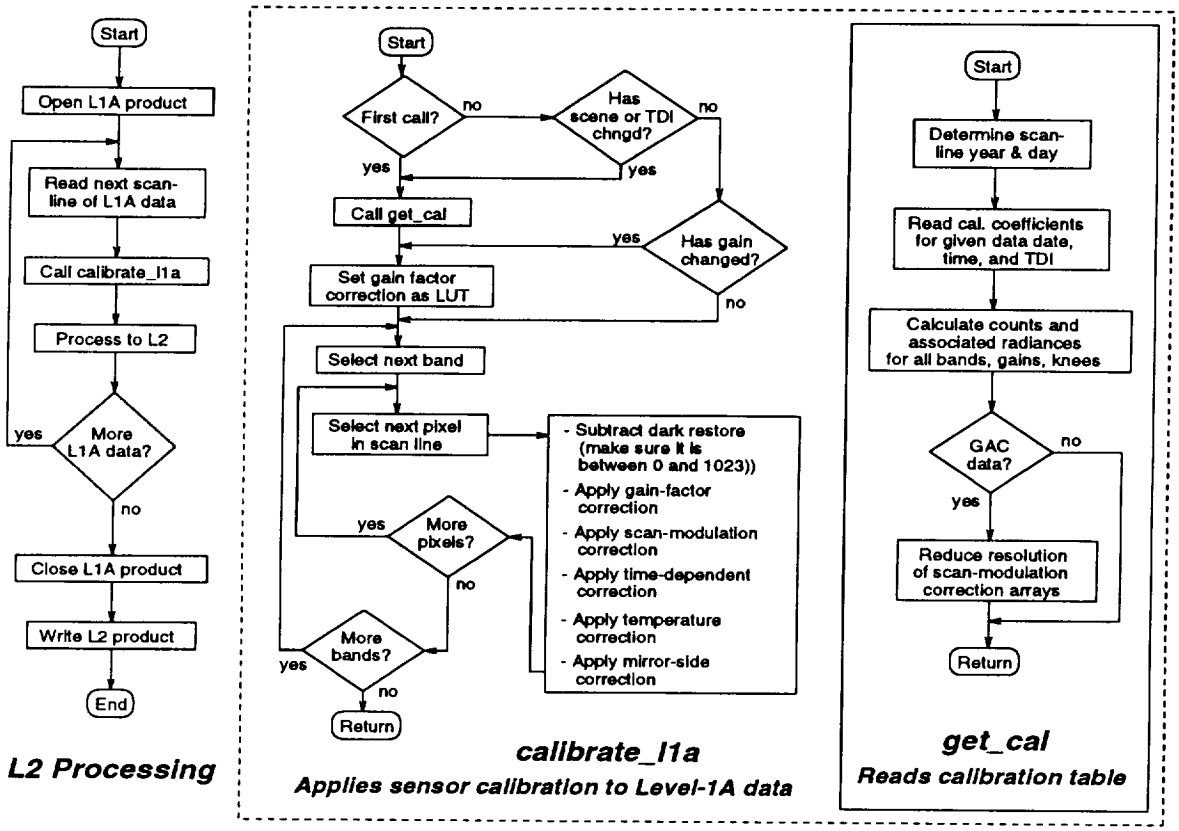

Fig. 10. Flow chart of the SeaWiFS operational sensor calibration procedure, showing idealized level-2 product generation steps, and the algorithms for the routines `calibrate_l1a` and `get_cal`, which are described in greater detail in the text.

- `dark_rest` (2-byte integer, array size 8): the dark restore (zero offset) for `l1a_data` values for all eight bands;
- `gain` (2-byte integer, array size 8): the gain values (0–3) for all eight bands;
- `tdi` (2-byte integer, array size 8): the time delay and integration (TDI) values for all eight bands (used by `get_cal`);
- `scan_temp` (2-byte integer, array size 8): the digitized scan temperatures for all eight bands;
- `side` (2-byte integer): the mirror side (0 or 1) of the scan line; and
- `l1a_data` (2-byte integer, array size 8×`nsamp`): the scan line of raw counts for all eight bands.

5.2.1.2 Output Arguments

The calibrated radiance values, and the date of entry to the calibration table, are returned by `calibrate_l1a` to the level-2 processing program:

- `cal_year` (2-byte integer): the year (4 digits) of each entry (i.e., update) to the calibration table, as returned by `get_cal`;
- `cal_day` (2-byte integer): the day of the year of each entry (i.e., update) to the calibration table, as returned by `get_cal`; and
- `l1b_data` (4-byte real, array size 8 × `nsamp`): the sensor calibrated radiance values corresponding to `l1a_data`.

5.2.1.3 Variables Returned By `get_cal`

The following variables are returned by `get_cal` for use by `calibrate_l1a`:

- `cal_year` (2-byte integer): the year (4 digits) of the entry (i.e., update) to the calibration table;
- `cal_day` (2-byte integer): the day of the year for the entry (i.e., update) to the calibration table;
- `temps` (4-byte real, array size 256 × 8): the temperature correction coefficients;
- `scan_mod` (4-byte real, array size 2 × 1,285): the scan modulation correction factors (the array dimensions represent *even/odd band number* × *pixels*); if `dtype` = `GAC`, then only the first 248 values of the *pixels* dimension are used;
- `mirror` (4-byte real, array size 2 × 8): the correction factors for mirror side 0 and mirror side 1 (the

dimension is computed from the number of sides times the number of bands);

- `time_factor`(4-byte real, array size 8): the time-dependent correction factors for all bands;
- `counts` (4-byte real, array size 8 × 4 × 5): the digital counts (zero-offsets corrected) corresponding to each calibration knee for all gains and bands (the dimension is computed from the number of bands times the number of gains times the number of knees); and
- `rads` (4-byte real, array size 8 × 4 × 5): the radiances corresponding to each calibration knee for all gains and bands (the dimension is computed from the number of bands times the number of gains times the number of knees).

5.2.1.4 Internal Variables

The following variables are used for processing within `calibrate_l1a`:

- `called_get_cal` (logical): used to check if `get_cal` has been called;
- `first_call` (logical): used to check if it is the first call to this routine (the initial value is `TRUE`);
- `band` (2-byte integer): an index for looping through bands;
- `knee` (2-byte integer): an index for looping through the knees of the bilinear gains;
- `n` (2-byte integer): a temporary counting variable;
- `count1` and `count2` (2-byte integers): used for the temporary storage of radiance counts;
- `slope` (4-byte real): used for temporary storage of the slope value from the function used to convert a level-1a count to radiance;
- `count` (2-byte integer): an index for looping through the possible radiance count values;
- `g_f` (4-byte real; array size 8 × 1024): the values in the look-up table (LUT) containing the gain factors for a given `gain` for all count values and all eight bands;
- `pixel` (2-byte integer): an index for looping through the pixels in a scan line; and
- `l1_data` (2-byte integer): used for the temporary storage of a dark restore-corrected count.

5.2.2 Algorithm

This section presents the `calibrate_l1a` algorithm using a combination of pseudocode and associated narrative comments.

5.2.2.1 Initialization

The routine `calibrate_l1a` calls `get_cal` to get the calibration parameters (corresponding to the date and time of the data and the TDI) if any of the following three situations occur:

1. It is the first call to `calibrate_l1a`.
2. The scene start date or start time has changed from the previous call to `calibrate_l1a`, indicating a new scene. In this case, the new scene may belong to a different time range in the sensor calibration table. [Note `get_cal` is not called if the scan line time variable (`msec`) changes, since it will change with every scan line; thus, some data for a scene located at the limits of a range will extend into another entry's time range. In effect, this logic assumes the sensor calibration does not change during a scene.]
3. The TDI has changed. In this case, new values of `counts` and `rads`, which are functions of TDI, must be obtained. The other parameters will also be reread, even though they do not change.

The following logic is for calling `get_cal`:

```
called_get_cal = FALSE
if (first_call) or (syear or sday or smsec
                or tdi has changed from previous call)
then
   first_call = FALSE
   save syear, sday, smsec, and tdi for next call
   call get_cal: get cal_year, cal_day, temps, scan_mod,
                 mirror, time_factor, counts, rads
   called_get_cal = TRUE
end if
```

The following logic sets up the gain factor LUT. This procedure is done to avoid the interpolation that would otherwise be needed with each pixel for the bilinear gains. The `do while` loop accounts for knees having the same saturation counts, which results from certain TDI combinations with duplicate detectors.

```
if (called_get_cal) or (gain has changed
                    from previous call) then
   save gain for next call
   do band = 0 to 7
      do knee = 1 to 4
         n = 1
         do while ((counts(band,gain(band),knee)=
                  counts(band,gain(band),knee-n)) and
                  (n=<k)
            n = n + 1
         end do while
         count1 = counts(band,gain(band),knee-n)
         count2 = counts(band,gain(band),knee)
         if knee = 4, count2 = 1023
         slope = (rads(band,gain(band),knee)-
                  rads(band,gain(band),knee-n))/
                  (counts(band,gain(band),knee)-
                   counts(band,gain(band),knee-n))
         do count = count1 to count2
            g_f(band,count) = slope *
               (count-counts(band,gain(band),knee-n))+
               rads(band,gain(band),knee-n)
         end do
      end do
   end do
end if
```

5.2.2.2 Application of Sensor Calibration

The highest looping structure cycles through the eight bands.

```
do for band = 0 to 7
```

The next loop cycles through the pixels of the scan line. Note that although `st_samp` and `nsamp` need not represent an entire scan line of pixels, the pixels must be consecutive pixels of a scan line because the scan modulation correction factor array assumes such an arrangement.

```
    do for pixel = st_samp-1 to st_samp+nsamp-2
```

The following logic is to correct for dark restore. Note that since the temporary value `l1_data` is used as an index, its value is forced to lie between 0-1,023, to account for the possibility that either the dark restore of the scan line is greater than `l1a_data`, or that the raw count values are corrupted.

```
        l1_data = l1a_data(band,pixel) - dark_rest(band)
        if l1_data < 0, l1_data = 0
        if l1_data > 1023, l1_data = 1023
```

This line of code retrieves the corresponding radiance from the gain factor LUT.

```
l1b_data(band,pixel) = g_f(band,l1_data)
```

First, the scan modulation correction is applied. The modular arithmetic function (`mod`) is used to determine if the even- or odd-band correction values should be used.

```
        l1b_data(band,pixel) =
         l1b_data(band,pixel) * scan_mod(mod(band,2),pixel)
```

Next, the time-dependent correction is applied.

```
        lib_data(band,pixel) =
           l1b_data(band,pixel) * time_factor(band)
```

Then the temperature correction is applied, using the byte `scan_temp` value as an index to look up the temperature correction factor.

```
        l1b_data(band,pixel) =
         l1b_data(band,pixel)*temps(scan_temp(band),band))
```

Finally, the mirror correction factor, for the mirror side corresponding to the scan line, is applied.

```
        l1b_data(band,pixel) =
           l1b_data(band,pixel) * mirror(side,band)
    end do
end do
return
```

5.3 THE get_cal ALGORITHM

The sensor calibration table is accessed operationally during the generation of level-2 products. The sensor calibration table read routine, `get_cal`, will open the sensor calibration table file, retrieve the sensor calibration data, and close the file during each call. The routine will return, for specified time and TDI values, the breakpoints (which are also called *knees*) in the band response function for each band and gain. The routine also returns the temperature and mirror side correction terms. The interface specifications for this routine are given in the interface specifications document authored by M. Darzi.

5.3.1 Variables

The following subsections define the variables used in the pseudocode of the `get_cal` algorithm (which is described in Section 5.3.2).

5.3.1.1 Input Arguments

The variables that follow provide data required by the `get_cal` algorithm, and therefore, comprise its input arguments as passed by `calibrate_l1a`:

- `cal_path` (character): the directory path and filename for the sensor calibration table file;
- `syear` (2-byte integer): the year (4 digits) of the scene start time;
- `sday` (2-byte integer): the day of the year for the scene start time;
- `eday` (2-byte integer): the day of the year for the scene end time;
- `msec` (4-byte real): the milliseconds of the day for the scan start time;
- `dtype` (character): the data type flag (i.e., GAC or LAC); and
- `tdi` (2-byte integer, array size 8): the time TDI values (0–255) for all eight bands, where the values represent the indices used to obtain the corresponding detector combinations from a LUT.

5.3.1.2 Output Arguments

The following variables are returned by `get_cal` to `calibrate_l1a`.

- `cal_year` (2-byte integer): the year (4 digits) of entry, i.e., update, to the calibration table;
- `cal_day` (2-byte integer): the day of the year of entry, i.e., update, to the calibration table;
- `temps` (4-byte real, array size 256 × 8): the temperature correction coefficients for calibration of the eight bands, read from the sensor calibration table file;
- `scan_mod` (4-byte real, array size 2 × 1285): the scan modulation correction factors,which are read from the sensor calibration table file (the array dimensions represent *even/odd band number* × *pixels*)—if `dtype` = 'GAC', then only the first 248 values of the *pixels* dimension are used;
- `mirror` (4-byte real, array size 2 × 8): the mirror side 0 and mirror side 1 correction factors, read from the sensor calibration file;

- `time_factor` (4-byte real, array size 8): the time-dependent correction factors for all bands; read from the sensor calibration table file;
- `counts` (4-byte real, array size 8 × 4 × 5): the digital counts (zero-offsets corrected) corresponding to each calibration knee for all gains and bands (dimensions = bands × gains × knees); and
- `rads` (4-byte real, array size 8 × 4 × 5): the radiances corresponding to each calibration knee for all gains and bands (dimensions = bands × gains × knees).

5.3.1.3 Internal Variables

The following variables are used for processing within `get_cal`.

- `dday` (2-byte integer): the scan line day of the year;
- `dyear` (2-byte integer): the scan line year (4 digits);
- `band` (2-byte integer): the index for looping through bands;
- `det` (2-byte integer): the index for looping through detectors;
- `dets` (2-byte integer, array size 4): an array for storing the combination of detector indices for a given TDI;
- `TDI_list` (2-byte integer, array size 256 × 4): TDI values (the array dimensions is computed from the number of detector combinations times the number of detectors);
- `gain` (2-byte integer): the index for looping through the gains;
- `scnts` (2-byte integer, array size 4): the saturation counts for the four-detector combination;
- `offs` (2-byte integer, array size 8×4): the zero-offset counts (dimensions are bands × detectors), read from the sensor calibration table file;
- `srads` (4-byte real, array size 4): the saturation radiances for the four-detector combination.
- `slopes` (4-byte real, array size 8×4×4): radiance-to-count slopes (the array dimension is computed from the number of bands times the number of gains times the number of detectors), read from the sensor calibration table file;
- `loc_slopes` (4-byte real, array size 4): a temporary storage array of the four-detector combination slopes;
- `oindex` (2-byte integer, array size 4): the indices of the four-detector combination arranged in ascending order of saturation radiances; and
- `pixel` (2-byte integer): the index for looping through an array that is the length of a scan line.

5.3.2 Algorithm

This section presents the `get_cal` algorithm using pseudocode and associated narrative comments.

5.3.2.1 Read Sensor Calibration Table File

First, `get_cal` determines the day and year of the scan line. This logic is needed to test and account for the possibility that the scene crosses a day boundary [2400 GMT], and the possibility that it crosses a year boundary, i.e., the end of a year.

```
dday = sday
dyear = syear
if sday <> eday and msec < 43.2E6 then
   dday = eday
   if dday = 1, dyear = syear + 1
end if
```

Then the sensor calibration table file is read. The routine will get data for the most recent entry in the table whose time range includes the satellite data date and time.

```
open file cal_path
read scan_mod, temps, and TDI_list
for the most recent entry whose time range includes dyear,
dday, and msec,
    read cal_year, cal_day, mirror, time_factor, slopes,
and offs
close file cal_path
```

5.3.2.2 Set Up Return Arrays

The highest looping structure cycles through the eight bands.

```
do for band = 0 to 7
```

For each band, the detector combination is determined from the TDI value.

```
   do for det = 0 to 3
      dets(det) = TDI_list(tdi(band),det) - 1
   end do
```

The routine then cycles through each of the four commandable gains.

```
   do gain = 0 to 3
```

The saturation counts and corresponding radiances for each detector are determined.

```
      do for det = 0 to 3
         scnts(det) = 1023 - offs(band,dets(det))
      srads(det) = scnts(det)*slopes(band,gain,dets(det))
         loc_slopes(det) = slopes(band,gain,dets(det))
      end do
```

The arrays are sorted according to saturation radiances.

```
      sort the detectors by saturation radiances
      place ordered indices of saturation radiances
         into oindex
```

The radiances of the knees (end points and three break points) of the gain response function are set in ascending order.

```
      rads(band,gain,0) = 0.0
      rads(band,gain,1) = srads(oindex(1))
      rads(band,gain,2) = srads(oindex(2))
      rads(band,gain,3) = srads(oindex(3))
      rads(band,gain,4) = srads(oindex(4))
```

The counts of the knees of the gain response function are set in ascending order.

```
      counts(band,gain,0) = 0
      counts(band,gain,1) = (scnts(oindex(0)) +
         srads(oindex(0))/loc_slopes(oindex(1)) +
         srads(oindex(0))/loc_slopes(oindex(2)) +
         srads(oindex(0))/loc_slopes(oindex(3))) / 4.0
      counts(band,gain,2) = (scnts(oindex(0)) +
                             scnts(oindex(1)) +
         srads(oindex(1))/loc_slopes(oindex(2)) +
         srads(oindex(1))/loc_slopes(oindex(3))) / 4.0
      counts(band,gain,3) = (scnts(oindex(0)) +
                             scnts(oindex(1)) +
                             scnts(oindex(2)) +
         srads(oindex(2))/loc_slopes(oindex(3))) / 4.0
      counts(band,gain,4) = (scnts(oindex(0)) +
                             scnts(oindex(1)) +
                             scnts(oindex(2)) +
                             scnts(oindex(3))) / 4.0
   end do
end do
```

Finally, for GAC data, the scan-modulation correction factor array is subsampled accordingly. These factors are stored in the sensor calibration table for an entire LAC scan line.

```
if dtype = GAC
   do pixel = 0 to 247
      scan_mod(1,pixel) = scan_mod(1,146+4*pixel)
      scan_mod(2,pixel) = scan_mod(2,146+4*pixel)
   end do
end if
return
```

5.4 SENSOR CALIBRATION TABLE

The sensor calibration table is comprised of a set of parameters which are required for applying the sensor calibration to raw, i.e., level-1a, data. The table is stored as a Hierarchical Data Format (HDF) file that is available as a SeaWiFS product. For operational use, the file is read by the `get_cal` routine. Figure 11 presents a schematic view of the data organization in the file. (See the sensor calibration table product specifications in Darzi et al. (1995) for the complete details of the HDF file structure of the file and a complete listing of the metadata and data parameters.)

The sensor calibration table includes parameters that will not be changed, as well as parameters which may be periodically updated. Updates are performed by the SeaWiFS Project and result in the appending of data to the file's contents—no data are deleted. Whenever the table is updated, a new version of the file is made available as a SeaWiFS product. Results of vicarious calibration studies may indicate if updates are needed to improve previous calibration parameter values, or to account for changes in sensor characteristics.

5.4.1 Parameters Containing Constants

The values of the following arrays will not be modified. Although they are constant and could have been supplied by the read routine itself, they are included in the sensor calibration table file for completeness and convenience:

- `TDI_list` (2-byte integer, array size 256 × 4): TDI values (the array dimensions = number of detector combinations × detectors);
- `temps` (4-byte real, array size 256 × 8): the temperature correction coefficients (the array dimensions represent the digitized temperature × bands); and
- `scan_mod` (4-byte real, array size 2 × 1,285): the scan modulation correction factors (the array dimensions = the even or odd band number × pixels).

5.4.2 Updatable Parameters

When the sensor calibration is *updated*, a new entry is appended to the end of each of the updatable parameters. An entry, therefore, consists of the values entered for all of the following parameters as part of an update. Each entry is associated with a time range specified as part of that entry. A time range defines a period of time corresponding to SeaWiFS data for which that entry's calibration parameter values apply.

A newly-entered time period will supersede part, or all, of one or more previously entered time periods. Only one period at a time is allowed to have an open end limit, to indicate that the period includes the most recent satellite data. If a new entry is made with an open-ended period, any such previous entry is modified such that the end of its period is set to just prior the start of the newly-entered period.

5.4.2.1 Parameters to Identify Entries

The `get_cal` routine will always obtain data from the most recent entry whose time period, defined by `Start Date/Time` and `End Date/Time`, includes the scan line's date and time. Note that the parameters described in this subsection are conceptual, and are not the actual names of the HDF data objects in the sensor calibration table [see the sensor calibration table product specifications in Darzi et al. (1995) for complete details].

- `Entry Date`: contains the year and the day of the year that the entry is made;
- `Start Date/Time`: contains the year, the day of the year, and the milliseconds of the day for the start of the time period for which the corresponding calibration entry applies; and
- `End Date/Time`: contains the year, the day of the year, and the milliseconds of the day for the end of the time period for which the corresponding calibration entry applies; if the values in `End Date/Time` are equal to 0, this indicates that no end to the time

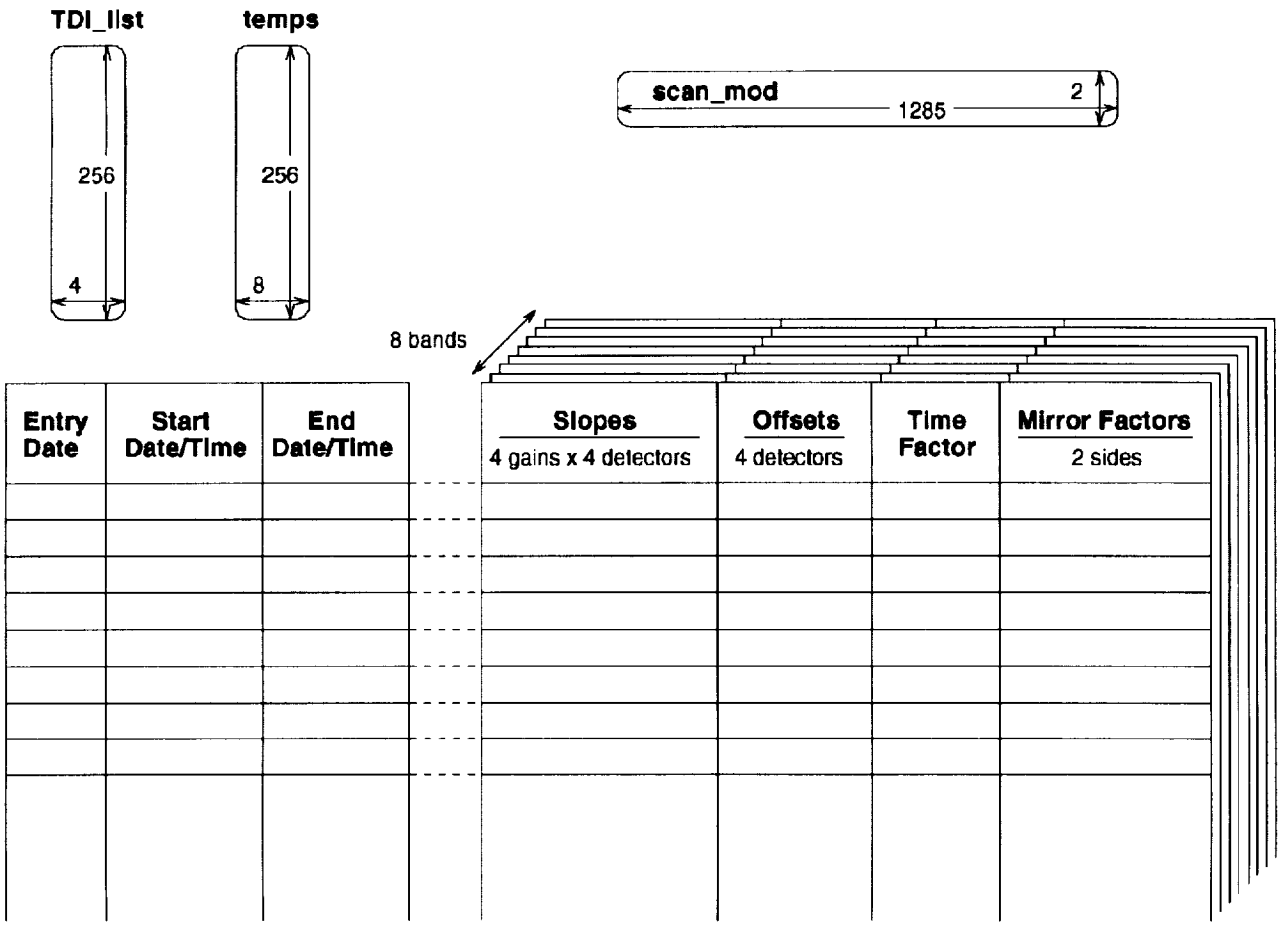

Fig. 11. Schematic view of the sensor calibration table, showing arrays of constant parameters (curved-corner rectangles), and updatable parameters in a tabular format.

period of the entry is specified, and that the entry applies up to the most recent satellite data.

5.4.2.2 Parameters Entered for Each Band

Note that the parameters described in this subsection are also conceptual (as in Section 5.4.2.1), and are not the actual names of the HDF data objects in the sensor calibration table [see the sensor calibration table product specifications in Darzi et al. (1995) for complete details].

- `Slopes` (4-byte real): the radiance-to-count slopes. Each band has a set of 16 values for each gain and detector combination (4×4), which are read into the array `slopes` by `get_cal`;
- `Offsets` (2-byte integer): the zero-offset counts. Each band has a set of 4 values for each detector, which are read into the array `offs` by `get_cal`;
- `Time Factor` (4-byte real): the time-dependent correction factor. Each band has one value, which is read into the array `time_factor` by `get_cal`; and
- `Mirror Factors` (4-byte real): the mirror correction factors. Each band has a set of 2 values for each mirror side which are read into the array `mirror` by `get_cal`.

Appendix A

The following tables are taken from Barnes et al. (1994b). Table A-1 corresponds to Table 13 of the original document, and Table A-2 corresponds to Table 14 of the same document.

Table A-1. Band edges (half maximum wavelengths) and extended band edges (1% wavelengths) for SeaWiFS bands 1–8. The center wavelength is calculated from the upper and lower band edges. Results are given for three light sources: spectrally flat, 5,900 K blackbody, and 2,850 K blackbody. Results are also given for the interference filter only, and for the system level measurement using the monochromator as a light source.

Band	*Nominal Band Edges* [nm]	*Lower Extended Band Edge* [nm]	*Lower Band Edge* [nm]	*Center Wavelength* [nm]	*Upper Band Edge* [nm]	*Upper Extended Band Edge* [nm]	*Source*
1	402–422	394.9	403.1	413.2	423.3	433.4	Spectrally Flat
		395.1	403.3	413.3	423.4	433.6	5,900 K
		395.9	404.5	414.1	423.7	434.8	2,850 K
		393.6	402.4	412.6	422.7	432.3	Filter Only†
		393.8	402.3	413.0	423.7	433.8	System Level§
2	433–453	424.0	434.1	443.9	453.7	463.7	Spectrally Flat
		424.1	434.2	444.0	453.8	463.7	5,900 K
		424.8	435.1	444.6	454.1	464.3	2,850 K
		423.3	433.5	443.5	453.5	464.6	Filter Only†
		422.3	433.6	444.1	454.6	463.8	System Level§
3	480–500	470.7	480.8	491.1	501.4	511.8	Spectrally Flat
		470.7	480.8	491.1	501.4	511.8	5,900 K
		471.3	481.5	491.6	501.6	512.3	2,850 K
		470.1	480.5	490.8	501.2	511.3	Filter Only†
		468.1	479.1	490.1	501.1	511.7	System Level§
4	500–520	488.1	498.9	510.1	521.3	530.7	Spectrally Flat
		488.1	498.9	510.1	521.2	530.7	5,900 K
		488.9	499.4	510.5	521.5	531.1	2,850 K
		487.8	498.7	509.9	521.0	532.9	Filter Only†
		487.2	498.6	510.3	522.0	530.9	System Level§
5	545–565	536.4	545.5	554.6	563.8	577.3	Spectrally Flat
		536.3	545.4	554.6	563.8	577.2	5,900 K
		536.9	545.8	554.9	563.9	577.9	2,850 K
		536.6	545.5	554.6	563.8	577.1	Filter Only†
		535.3	544.6	554.2	563.9	577.0	System Level§
6	660–680	646.8	658.3	668.2	678.2	692.7	Spectrally Flat
		646.7	658.3	668.2	678.1	692.5	5,900 K
		646.9	658.5	668.4	678.3	692.9	2,850 K
		646.8	658.4	668.3	678.2	692.8	Filter Only†
		646.2	658.8	668.8	678.8	692.2	System Level§
7	745–785	728.0	744.7	764.9	785.0	814.5	Spectrally Flat
		727.6	744.6	764.6	784.6	812.9	5,900 K
		728.4	745.1	765.1	785.1	815.6	2,850 K
		725.1	744.3	765.0	785.7	814.2	Filter Only†
		‡	743.3	763.8	784.2	‡	System Level§
8	845–885	826.7	845.7	866.4	887.0	908.2	Spectrally Flat
		826.4	845.5	866.1	886.7	907.5	5,900 K
		826.8	845.7	866.5	887.2	908.4	2,850 K
		826.5	845.6	866.2	886.9	908.0	Filter Only†
		‡	845.6	866.4	887.2	‡	System Level§

† Calculated from measurements of the narrow band interference filter only.

§ Calculated from system level measurements using a monochromator as the light source.

‡ Outside of the range of the system level measurements.

Table A-2. Calculated out-of-band responses for the eight SeaWiFS bands. The instrument responses are given as the output of the photodiode in picoamperes. The 5,900 K radiances in the calculations are normalized to the expected saturation radiance for each band at the nominal center wavelength for each band. The upper and lower extended band edges also come from Barnes et al. (1994b) in Tables 7 and 8. These results are calculated over the wavelength range from 380–1,150 nm.

Band	*Lower Out-of-Band Response* [pA]	*Lower Extended Band Edge* [nm]	*In-Band Response* [pA]	*Upper Extended Band Edge* [nm]	*Upper Out-of-Band Response* [pA]	*Out-of-Band Response* [%]
1	3.38	395.2	2,175.35	433.6	11.77	0.70
2	9.59	424.1	3,418.80	463.7	1.56	0.33
3	6.48	470.7	4,301.14	511.7	28.08	0.80
4	17.32	488.1	4,586.23	530.7	8.96	0.58
5	39.14	536.6	3,631.84	577.2	46.14	2.35
6	12.66	646.7	2,071.19	692.2	7.84	0.99
7	10.17	727.3	2,818.97	813.4	29.58	1.41
8	66.36	826.4	2,191.97	907.5	15.43	3.73

GLOSSARY

ASCII American Standard Code for Information Interchange

CVT Calibration and Validation Team
CZCS Coastal Zone Color Scanner

DAAC Distributed Active Archive Center

FPA Focal Plane Assembly

GAC Global Area Coverage
GMT Greenwich Mean Time
GSFC Goddard Space Flight Center

HDF Hierarchical Data Format

IR Infrared

LAC Local Area Coverage
LUT Look-Up Table

NASA National Aeronautics and Space Administration
NIMBUS Not an acronym, but representing a series of NASA experimental weather satellites carrying a wide variety of atmosphere, ice, and ocean sensors.

OCDM Ocean Color Data Mission

PST Postage Stamp (pixel size designation)

QC Quality Control

SBRC Santa Barbara Research Center
SDPS SeaWiFS Data Processing System
S/C Spacecraft
SEAPAK Not an acronym, but an image display and analysis package developed at GSFC.
SeaWiFS Sea-viewing Wide Field-of-view Sensor
SWG Science Working Group

TDI Time Delay and Integration
TIROS Television and Infrared Observation Satellite
TOMS Total Ozone Mapping Spectrometer
TOVS TIROS Operational Vertical Sounder

SYMBOLS

b_b Backscattering coefficient.
B Variable in the expression for limiting reflectance ($R_{\rm lim}$), defined as $0.33b/K_d$.

C Chlorophyll concentration.

$F_0(\lambda)$ Extraterrestrial solar irradiance.

K_d Diffuse attenuation coefficient for downwelling irradiance.
$K(440)$ Diffuse attenuation coefficient at 440 nm.

L_a Aerosol radiance.
L_g Glint radiance.
L_i Incident light.
$L_t(\lambda)$ Total radiance.
$L_W(\lambda)$ Water-leaving radiance.
$L_{WN}(\lambda)$ Normalized water-leaving radiance.

n The index of refraction.

P_W Probability of seeing sun glint in the spacecraft direction.

Q The ratio of upwelling irradiance to radiance, which varies with the angular distribution of the upwelling light field, and is π for an isotropic distribution.

$R_{\rm lim}$ Limiting reflectance for defining Case-1 water.
R_{rs} Remote sensing reflectance.

$t(750, \theta)$ Diffuse transmittance between the ocean surface and the sensor at 750 nm.
$T_0(\lambda, \theta_0)$ Total downward transmittance of irradiance.

W Wind speed.

α_{750} Albedo at 750 nm.

ϵ Atmospheric correction parameter.

θ Spacecraft zenith angle.
θ_0 Solar zenith angle.

λ Wavelength.

ρ Fresnel reflectivity.

τ_a Aerosol radiance.
τ_{ox} Oxygen optical thickness.
τ_{oz} Ozone optical thickness.
τ_r Rayleigh optical thickness.

ϕ Azimuth angle at the line-of-sight of a spacecraft.
ϕ_0 Azimuth angle of direct sunlight.

REFERENCES

Ackleson S.G., and P.M. Holligan, 1989: AVHRR observations of a Gulf of Maine coccolithophorid bloom. *Photogramm. Eng. Remote Sens.,* **55,** 473–474.

Aiken, J., G.F. Moore, and P.M. Holligan, 1992: Remote sensing of oceanic biology in relation to global climate change. *J. Phycol.,* **28,** 579–590.

Allen, C.W., 1973: *Astrophysical Quantities, 3rd Edition.* Athalone Press, London, 310 pp.

Arrigo, K.R., and C.R. McClain, 1995: "Cloud and ice detection at high latitudes for processing of CZCS imagery," In: McClain, C.R., W.E. Esaias, M. Darzi, F.S. Patt, R.H. Evans, J.W. Brown, K.R. Arrigo, C.W. Brown, R.A. Barnes, and L. Kumar, 1995: Case Studies for SeaWiFS Calibration and Validation, Part 4. *NASA Tech. Memo. 104566, Vol. 28,* S.B. Hooker, E.R. Firestone, and J.G. Acker, Eds., NASA Goddard Space Flight Center, 8–12.

Balch, W.M., P.M. Holligan, S.G. Ackleson, and K.J. Voss, 1991: Biological and optical properties of mesoscale coccolithophore blooms in the Gulf of Maine. *Limnol. Oceanogr.,* **36,** 629–643.

Barnes, R.A., W.L. Barnes, W.E. Esaias, and C.L. McClain, 1994a: Prelaunch Acceptance Report for the SeaWiFS Radiometer. *NASA Tech. Memo. 104566, Vol. 22,* S.B. Hooker, E.R. Firestone, and J.G. Acker, Eds., NASA Goddard Space Flight Center, Greenbelt, Maryland, 32 pp.

——, A.W. Holmes, W.L. Barnes, W.E. Esaias, and C.R. McClain, 1994b: SeaWiFS Prelaunch Radiometric Calibration and Spectral Characterization. *NASA Tech. Memo. 104566, Vol. 23,* S.B. Hooker, E.R. Firestone, and J.G. Acker, Eds., NASA Goddard Space Flight Center, Greenbelt, Maryland, 55 pp.

Bricaud, A., and A. Morel, 1987: Atmospheric corrections and interpretation of marine radiances in CZCS imagery: Use of a reflectance model. *Oceanol. Acta,* **7,** 33–50.

Brown, C.W., 1995: "Classification of coccolithophore blooms in ocean color imagery." In: McClain, C.R., W.E. Esaias, M. Darzi, F.S. Patt, R.H. Evans, J.W. Brown, K.R. Arrigo, C.W. Brown, R.A. Barnes, and L. Kumar, 1995: Case Studies for SeaWiFS Calibration and Validation, Part 4. *NASA Tech. Memo. 104566, Vol. 28,* S.B. Hooker, E.R. Firestone, and J.G. Acker, Eds., NASA Goddard Space Flight Center, Greenbelt, Maryland, 13–19.

——, and J.A. Yoder, 1994a: Coccolithophorid blooms in the global ocean. *J. Geophys. Res.,* **99,** 7,467–7,482.

——, and ——, 1994b: Distribution pattern of coccolithophorid blooms in the western North Atlantic. *Cont. Shelf Res.,* **14,** 175–198.

Carder, K.L., W.W. Gregg, D.K. Costello, K. Haddad, and J.M. Prospero, 1991: Determination of Saharan dust radiance and chlorophyll from CZCS imagery. *J. Geophys. Res.,* **96,** 5,369–5,378.

Cox, C., and W. Munk, 1954: Statistics of the sea surface derived from sun glitter. *J. Mar. Res.,* **13,** 198–277.

Darzi, M., 1992: Cloud Screening for Polar Orbiting Visible and Infrared (IR) Satellite Sensors. *NASA Tech. Memo. 104566, Vol. 7,* S.B. Hooker and E.R. Firestone, Eds., NASA Goddard Space Flight Center, Greenbelt, Maryland, 7 pp.

Darzi, M., F.S. Patt, J.K. Firestone, B. Schieber, L. Kumar, and D. Ilg, 1995: *SeaWiFS Operational Archive Product Specifications.* [World Wide Web page.] From URL: `http://seawifs.gsfc.nasa.gov/SEAWIFS/SOFTWARE/SOFTWARE.html` see "SeaWiFS Product Specifications (postscript)". NASA Goddard Space Flight Center, Greenbelt, Maryland.

Duntley, S.Q., R.W. Austin, W.H. Wilson, C.F. Edgerton, and M.E. Moran, 1974: Ocean color analysis. *Visibility Laboratory of the Scripps Institution of Oceanography Report, SIO Ref. 74-10,* 70 pp.

Eckstein, B.A., and J.J. Simpson, 1991: Cloud screening Coastal Zone Color Scanner images using channel 5. *Int. J. Remote Sens.,* **12,** 2,359–2,377.

Evans, R.H., and H.R. Gordon, 1994: CZCS "system calibration": A retrospective examination. *J. Geophys. Res.,* **99,** 7,293–7,307.

Feldman, G., N. Kuring, C. Ng, W. Esaias, C. McClain, J. Elrod, N. Maynard, D. Endres, R. Evans, J. Brown, S. Walsh, M. Carle, and G. Podesta, 1989: Ocean color: Availability of the global data set. *Eos, Trans. AGU,* **70,** 634.

Firestone, E.R., and S.B. Hooker, 1995: SeaWiFS Technical Report Series Cumulative Index: Volumes 1–17, *NASA Tech. Memo. 104566, Vol. 18,* S.B. Hooker and E.R. Firestone Eds., NASA Goddard Space Flight Center, Greenbelt, Maryland, 16–18.

Gallaudet, T.C., and J.J. Simpson, 1991: Automated cloud screening of AVHRR imagery using split-and-merge clustering. *Remote Sens. Environ.,* **38,** 77–121.

Gordon, H.R., and D.K. Clark, 1981: Clear water radiances for atmospheric correction of Coastal Zone Color Scanner imagery. *Appl. Opt.,* **20,** 4,175–4,180.

——, and A.Y. Morel, 1983: Remote assessment of ocean color for interpretation of satellite visible imagery: review. *Lecture Notes on Coastal and Estuarine Studies, Vol. 4,* Springer-Verlag, 114 pp.

——, D.K. Clark, J.W. Brown, O.B. Brown, R.H. Evans, and W.W. Broenkow, 1983: Phytoplankton pigment concentrations in the Middle Atlantic Bight: Comparison of ship determinations and CZCS estimates. *Appl. Opt.,* **22,** 20–36.

——, J.W. Brown, and R.H. Evans, 1988a: Exact Rayleigh scattering calculations for use with the Nimbus-7 Coastal Zone Color Scanner. *Appl. Optics,* **27,** 862–871.

——, O.B. Brown, R.H. Evans, J.W. Brown, R.C. Smith, K.S. Baker, and D.K. Clark, 1988b: A semianalytic radiance model of ocean color. *J. Geophys. Res.,* **93,** 10,909–10,924.

——, and M. Wang, 1994: Retrieval of water-leaving radiance and aerosol optical thickness over the oceans with SeaWiFS: a preliminary algorithm. *Appl. Opt.,* **33,** 443–452.

Gregg, W.W., F.C. Chen, A.L. Mezaache, J.D. Chen, and J.A. Whiting, 1993: The Simulated SeaWiFS Data Set, Version 1. *NASA Tech. Memo. 104566, Vol. 9,* S.B. Hooker, E.R. Firestone, and A.W. Indest, Eds., NASA Goddard Space Flight Center, Greenbelt, Maryland, 17 pp.

Holligan, P.M., M. Viollier, D.S. Harbour, P. Camus, and M. Champagne-Philippe, 1983: Satellite and ship studies of coccolithophore production along a continental shelf edge. *Nature,* **304,** 339–342.

——, and W.M. Balch, 1991: From the ocean to cells: coccolithophore optics and biogeochemistry. *Particle Analysis in Oceanography,* S. Demers, Ed., Springer-Verlag, Berlin, 301–324.

——, E. Fernandez, J. Aiken, W.M. Balch, P. Boyd, P.H. Burkill, M. Finch, S.B. Groom, G. Malin, K. Muller, D.A. Purdie, C. Robinson, C.C. Trees, S.M. Turner, and P. van der Wal, 1993: A biogeochemical study of the coccolithophore, *Emiliania huxleyi,* in the North Atlantic. *Global Biogeochem. Cycles,* **7,** 879–900.

Hooker, S.B., W.E. Esaias, G.C. Feldman, W.W. Gregg, and C.R. McClain, 1992: An Overview of SeaWiFS and Ocean Color, *NASA Tech. Memo. 104566, Vol. 1,* S.B. Hooker and E.R. Firestone, Eds., NASA Goddard Space Flight Center, Greenbelt, Maryland, 25 pp., plus color plates.

Martin, D.L., 1992: *Minimizing Systematic Errors in Phytoplankton Pigment Concentration Derived from Satellite Ocean Color Measurements.* Ph.D. dissertation, University of Washington, Seattle, Washington, 121 pp.

McClain, C.R., M. Darzi, J. Firestone, E-n. Yeh, G. Fu, and D. Endres, 1991: SEAPAK User's Guide, Version 2.0, Vol. II—Descriptions of Programs. *NASA Tech. Memo. 100728,* NASA Goddard Space Flight Center, Greenbelt, Maryland, 158 pp.

——, W.E. Esaias, W. Barnes, B. Guenther, D. Endres, S.B. Hooker, B.G. Mitchell, and R. Barnes, 1992: SeaWiFS Calibration and Validation Plan. *NASA Tech. Memo. 104566, Vol. 3,* S.B. Hooker and E.R. Firestone, Eds., NASA Goddard Space Flight Center, Greenbelt, Maryland, 41 pp.

——, G. Feldman, and W. Esaias, 1993: Oceanic biological productivity. *Atlas of Ssatellite Observations Related to Global Change,* R.J. Gurney, J.L. Foster, and C.L. Parkinson, Eds., Cambridge University Press, 251–263.

——, R.S. Fraser, and E-n. Yeh, 1994: "SeaWiFS Pressure and Oxygen Absorption Study," In: McClain, C.R., J.C. Comiso, R.S. Fraser, J.K. Firestone, B.D. Schieber, E-n. Yeh, K.R. Arrigo, C.W. Sullivan, 1994: Case Studies for SeaWiFS Calibration and Validation, Part 1. *NASA Tech. Memo. 104566, Vol. 13,* S.B. Hooker and E.R. Firestone, Eds., NASA Goddard Space Flight Center, Greenbelt, Maryland, 15–20.

——, and E-n. Yeh, 1994a: "Pixel-by-pixel pressure and ozone correction study," In: McClain, C.R., J.C. Comiso, R.S. Fraser, J.K. Firestone, B.D. Schieber, E-n. Yeh, K.R. Arrigo, C.W. Sullivan, 1994: Case Studies for SeaWiFS Calibration and Validation, Part 1. *NASA Tech. Memo. 104566, Vol. 13,* S.B. Hooker and E.R. Firestone, Eds., NASA Goddard Space Flight Center, Greenbelt, Maryland, 21–26.

——, and ——, 1994b: "Sun glint flag sensitivity study," In: McClain, C.R., J.C. Comiso, R.S. Fraser, J.K. Firestone, B.D. Schieber, E-n. Yeh, K.R. Arrigo, C.W. Sullivan, 1994: Case Studies for SeaWiFS Calibration and Validation, Part 1. *NASA Tech. Memo. 104566, Vol. 13,* S.B. Hooker and E.R. Firestone, Eds., NASA Goddard Space Flight Center, Greenbelt, Maryland, 49–50.

Morel, A., 1988: Optical modeling of the upper ocean in relation to its biogenous matter content (Case I waters). *J. Geophys. Res.,* **93,** 10,749–10,768.

Robbins, L.L., and P.L. Blackwelder, 1992: Biochemical and ultrastructural evidence for the origin of whitings: A biologically induced calcium carbonate precipitation mechanism. *Geology,* **20,** 464–468.

Schowengerdt, R.A., 1983: *Techniques for Image Processing and Classification in Remote Sensing.* Academic Press, 249 pp.

Subramaniam, A., and E.J. Carpenter, 1994: An empirically derived protocol for the detection of blooms of the marine cyanobacterium *Trichodesmium* using CZCS imagery. *Int. J. Remote Sens.,* **15,** 1,559–1,569.

Shinn, J.A., R.P. Steinen, B.H. Lidz, and P.K. Swart, 1989: Whitings, a sedimentologic dilemma. *J. Sed. Petrol.,* **59,** 147–161.

Toratani, M., and H. Fukushima, 1993: Atmospheric correction scheme for ocean color remote sensing in consideration to Asian dust aerosol. *IGARSS '93, Vol. 4,* IEEE, New York, 1,937–1,940.

Viollier, M., D. Tanreé, and P.Y. Deschamps, 1980: An algorithm for remote sensing of water color from space. *Bound.-Layer Meteor.,* **18,** 247–267.

Warneck, P., 1988: *Chemistry of the Natural Atmosphere.* Academic Press, 757 pp.

The SeaWiFS Technical Report Series

Vol. 1

Hooker, S.B., W.E. Esaias, G.C. Feldman, W.W. Gregg, and C.R. McClain, 1992: An Overview of SeaWiFS and Ocean Color. *NASA Tech. Memo. 104566, Vol. 1,* S.B. Hooker and E.R. Firestone, Eds., NASA Goddard Space Flight Center, Greenbelt, Maryland, 24 pp., plus color plates.

Vol. 2

Gregg, W.W., 1992: Analysis of Orbit Selection for SeaWiFS: Ascending vs. Descending Node. *NASA Tech. Memo. 104566, Vol. 2,* S.B. Hooker and E.R. Firestone, Eds., NASA Goddard Space Flight Center, Greenbelt, Maryland, 16 pp.

Vol. 3

McClain, C.R., W.E. Esaias, W. Barnes, B. Guenther, D. Endres, S. Hooker, G. Mitchell, and R. Barnes, 1992: Calibration and Validation Plan for SeaWiFS. *NASA Tech. Memo. 104566, Vol. 3,* S.B. Hooker and E.R. Firestone, Eds., NASA Goddard Space Flight Center, Greenbelt, Maryland, 41 pp.

Vol. 4

McClain, C.R., E. Yeh, and G. Fu, 1992: An Analysis of GAC Sampling Algorithms: A Case Study. *NASA Tech. Memo. 104566, Vol. 4,* S.B. Hooker and E.R. Firestone, Eds., NASA Goddard Space Flight Center, Greenbelt, Maryland, 22 pp., plus color plates.

Vol. 5

Mueller, J.L., and R.W. Austin, 1992: Ocean Optics Protocols for SeaWiFS Validation. *NASA Tech. Memo. 104566, Vol. 5,* S.B. Hooker and E.R. Firestone, Eds., NASA Goddard Space Flight Center, Greenbelt, Maryland, 43 pp.

Vol. 6

Firestone, E.R., and S.B. Hooker, 1992: SeaWiFS Technical Report Series Summary Index: Volumes 1–5. *NASA Tech. Memo. 104566, Vol. 6,* S.B. Hooker and E.R. Firestone, Eds., NASA Goddard Space Flight Center, Greenbelt, Maryland, 9 pp.

Vol. 7

Darzi, M., 1992: Cloud Screening for Polar Orbiting Visible and IR Satellite Sensors. *NASA Tech. Memo. 104566, Vol. 7,* S.B. Hooker and E.R. Firestone, Eds., NASA Goddard Space Flight Center, Greenbelt, Maryland, 7 pp.

Vol. 8

Hooker, S.B., W.E. Esaias, and L.A. Rexrode, 1993: Proceedings of the First SeaWiFS Science Team Meeting. *NASA Tech. Memo. 104566, Vol. 8,* S.B. Hooker and E.R. Firestone, Eds., NASA Goddard Space Flight Center, Greenbelt, Maryland, 61 pp.

Vol. 9

Gregg, W.W., F.C. Chen, A.L. Mezaache, J.D. Chen, J.A. Whiting, 1993: The Simulated SeaWiFS Data Set, Version 1. *NASA Tech. Memo. 104566, Vol. 9,* S.B. Hooker and E.R. Firestone, and A.W. Indest, Eds., NASA Goddard Space Flight Center, Greenbelt, Maryland, 17 pp.

Vol. 10

Woodward, R.H., R.A. Barnes, C.R. McClain, W.E. Esaias, W.L. Barnes, and A.T. Mecherikunnel, 1993: Modeling of the SeaWiFS Solar and Lunar Observations. *NASA Tech. Memo. 104566, Vol. 10,* S.B. Hooker and E.R. Firestone, Eds., NASA Goddard Space Flight Center, Greenbelt, Maryland, 26 pp.

Vol. 11

Patt, F.S., C.M. Hoisington, W.W. Gregg, and P.L. Coronado, 1993: Analysis of Selected Orbit Propagation Models for the SeaWiFS Mission. *NASA Tech. Memo. 104566, Vol. 11,* S.B. Hooker, E.R. Firestone, and A.W. Indest, Eds., NASA Goddard Space Flight Center, Greenbelt, Maryland, 16 pp.

Vol. 12

Firestone, E.R., and S.B. Hooker, 1993: SeaWiFS Technical Report Series Summary Index: Volumes 1–11. *NASA Tech. Memo. 104566, Vol. 12,* S.B. Hooker and E.R. Firestone, Eds., NASA Goddard Space Flight Center, Greenbelt, Maryland, 28 pp.

Vol. 13

McClain, C.R., K.R. Arrigo, J. Comiso, R. Fraser, M. Darzi, J.K. Firestone, B. Schieber, E-n. Yeh, and C.W. Sullivan, 1994: Case Studies for SeaWiFS Calibration and Validation, Part 1. *NASA Tech. Memo. 104566, Vol. 13,* S.B. Hooker and E.R. Firestone, Eds., NASA Goddard Space Flight Center, Greenbelt, Maryland, 52 pp., plus color plates.

Vol. 14

Mueller, J.L., 1993: The First SeaWiFS Intercalibration Round-Robin Experiment, SIRREX-1, July 1992. *NASA Tech. Memo. 104566, Vol. 14,* S.B. Hooker and E.R. Firestone, Eds., NASA Goddard Space Flight Center, Greenbelt, Maryland, 60 pp.

Vol. 15

Gregg, W.W., F.S. Patt, R.H. Woodward, 1994: The Simulated SeaWiFS Data Set, Version 2. *NASA Tech. Memo. 104566, Vol. 15,* S.B. Hooker and E.R. Firestone, Eds., NASA Goddard Space Flight Center, Greenbelt, Maryland, 42 pp., plus color plates.

Vol. 16

Mueller, J.L., B.C. Johnson, C.L. Cromer, J.W. Cooper, J.T. McLean, S.B. Hooker, and T.L. Westphal, 1994: The Second SeaWiFS Intercalibration Round-Robin Experiment, SIRREX-2, June 1993. *NASA Tech. Memo. 104566, Vol. 16,* S.B. Hooker and E.R. Firestone, Eds., NASA Goddard Space Flight Center, Greenbelt, Maryland, 121 pp.

Vol. 17

Abbott, M.R., O.B. Brown, H.R. Gordon, K.L. Carder, R.E. Evans, F.E. Muller-Karger, and W.E. Esaias, 1994: Ocean color in the 21st century: a strategy for a 20-year time series. *NASA Tech. Memo. 104566, Vol. 17,* S.B. Hooker and E.R. Firestone, Eds., NASA Goddard Space Flight Center, Greenbelt, Maryland, 20 pp.

Vol. 18

Firestone, E.R., and S.B. Hooker, 1995: SeaWiFS Technical Report Series Summary Index: Volumes 1–17. *NASA Tech. Memo. 104566, Vol. 18,* S.B. Hooker and E.R. Firestone, Eds., NASA Goddard Space Flight Center, Greenbelt, Maryland, 47 pp.

Vol. 19

McClain, C.R., R.S. Fraser, J.T. McLean, M. Darzi, J.K. Firestone, F.S. Patt, B.D. Schieber, R.H. Woodward, E-n. Yeh, S. Mattoo, S.F. Biggar, P.N. Slater, K.J. Thome, A.W. Holmes, R.A. Barnes, and K.J. Voss, 1994: Case Studies for SeaWiFS Calibration and Validation, Part 2. *NASA Tech. Memo. 104566, Vol. 19,* S.B. Hooker, E.R. Firestone, and J.G. Acker, Eds., NASA Goddard Space Flight Center, Greenbelt, Maryland, 69 pp.

Vol. 20

Hooker, S.B., C.R. McClain, J.K. Firestone, T.L. Westphal, E-n. Yeh, and Y. Ge, 1994: The SeaWiFS Bio-Optical Archive and Storage System (SeaBASS), Part 1. *NASA Tech. Memo. 104566, Vol. 20,* S.B. Hooker and E.R. Firestone, Eds., NASA Goddard Space Flight Center, Greenbelt, Maryland, 40 pp.

Vol. 21

Acker, J.G., 1994: The Heritage of SeaWiFS: A Retrospective on the CZCS NIMBUS Experiment Team (NET) Program. *NASA Tech. Memo. 104566, Vol. 21,* S.B. Hooker and E.R. Firestone, Eds., NASA Goddard Space Flight Center, Greenbelt, Maryland, 43 pp.

Vol. 22

Barnes, R.A., W.L. Barnes, W.E. Esaias, and C.R. McClain, 1994: Prelaunch Acceptance Report for the SeaWiFS Radiometer. *NASA Tech. Memo. 104566, Vol. 22,* S.B. Hooker, E.R. Firestone, and J.G. Acker, Eds., NASA Goddard Space Flight Center, Greenbelt, Maryland, 32 pp.

Vol. 23

Barnes, R.A., A.W. Holmes, W.L. Barnes, W.E. Esaias, C.R. McClain, and T. Svitek, 1994: SeaWiFS Prelaunch Radiometric Calibration and Spectral Characterization. *NASA Tech. Memo. 104566, Vol. 23,* S.B. Hooker, E.R. Firestone, and J.G. Acker, Eds., NASA Goddard Space Flight Center, Greenbelt, Maryland, 55 pp.

Vol. 24

Firestone, E.R., and S.B. Hooker, 1995: SeaWiFS Technical Report Series Summary Index: Volumes 1–23. *NASA Tech. Memo. 104566, Vol. 24,* S.B. Hooker and E.R. Firestone, Eds., NASA Goddard Space Flight Center, Greenbelt, Maryland, 36 pp.

Vol. 25

Mueller, J.L., and R.W. Austin, 1995: Ocean Optics Protocols for SeaWiFS Validation, Revision 1. *NASA Tech. Memo. 104566, Vol. 25,* S.B. Hooker and E.R. Firestone, Eds., NASA Goddard Space Flight Center, Greenbelt, Maryland, 67 pp.

Vol. 26

Siegel, D.A., M.C. O'Brien, J.C. Sorensen, D.A. Konnoff, E.A. Brody, J.L. Mueller, C.O. Davis, W.J. Rhea, and S.B. Hooker, 1995: Results of the SeaWiFS Data Analysis Round-Robin (DARR), July 1994. *NASA Tech. Memo. 104566, Vol. 26,* S.B. Hooker and E.R. Firestone, Eds., NASA Goddard Space Flight Center, Greenbelt, Maryland, 58 pp.

Vol. 27

Mueller, J.L., R.S. Fraser, S.F. Biggar, K.J. Thome, P.N. Slater, A.W. Holmes, R.A. Barnes, C.T. Weir, D.A. Siegel, D.W. Menzies, A.F. Michaels, and G. Podesta 1995: Case Studies for SeaWiFS Calibration and Validation, Part 3. *NASA Tech. Memo. 104566, Vol. 27,* S.B. Hooker, E.R. Firestone, and J.G. Acker, Eds., NASA Goddard Space Flight Center, Greenbelt, Maryland, 46 pp.

Vol. 28

McClain, C.R., K.R. Arrigo, W.E. Esaias, M. Darzi, F.S. Patt, R.H. Evans, J.W. Brown, C.W. Brown, R.A. Barnes, and L. Kumar, 1995: SeaWiFS Algorithms, Part 1. *NASA Tech. Memo. 104566, Vol. 28,* S.B. Hooker, E.R. Firestone, and J.G. Acker, Eds., NASA Goddard Space Flight Center, Greenbelt, Maryland, 38 pp., plus color plates.

COLOR PLATES

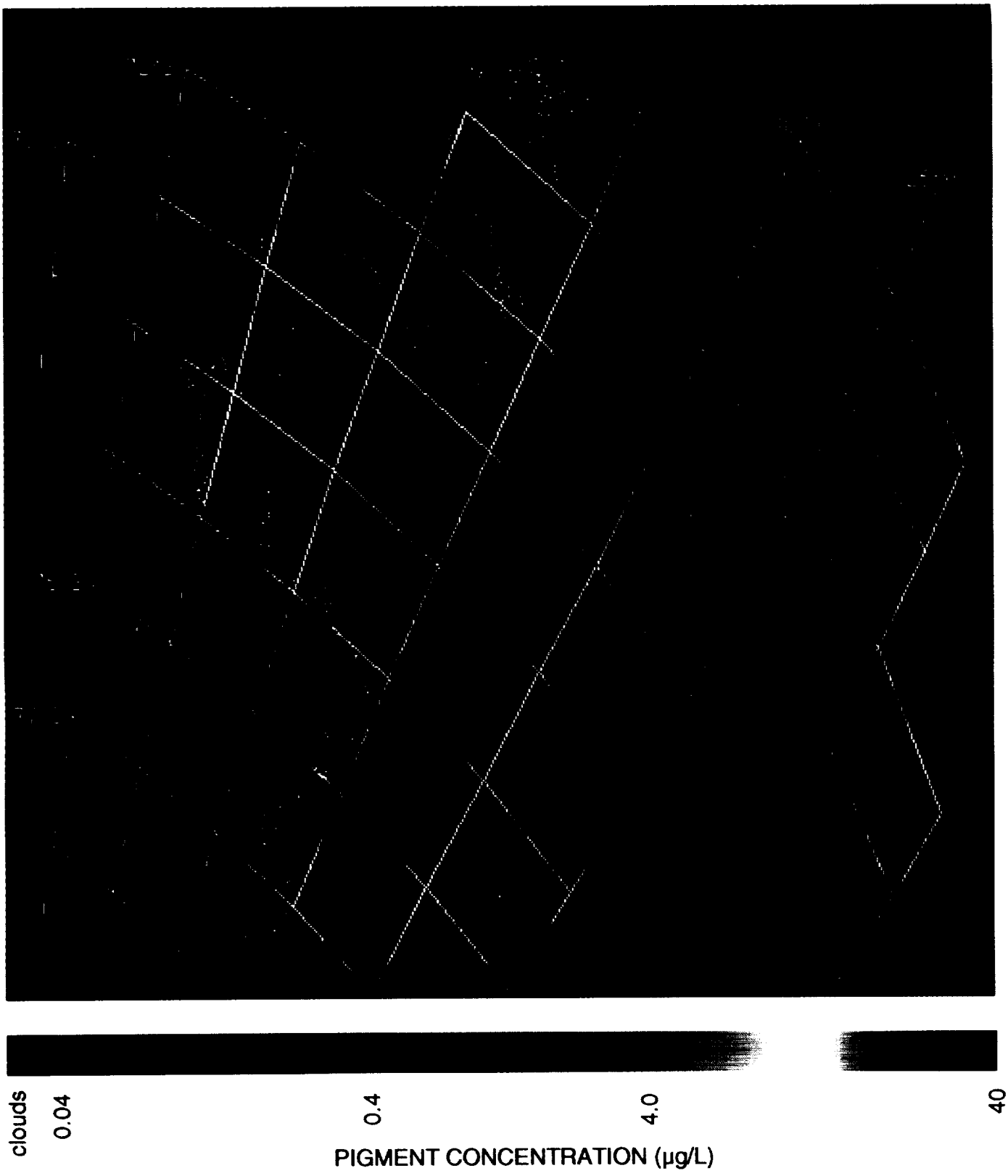

PLATE 1. Scene 1: CZCS pigment image from the western Weddell Sea for 1 March 1986. The image was processed assuming $\alpha_{750} = 1.6\%$, and using a bilinearly interpolated surface pressure field.

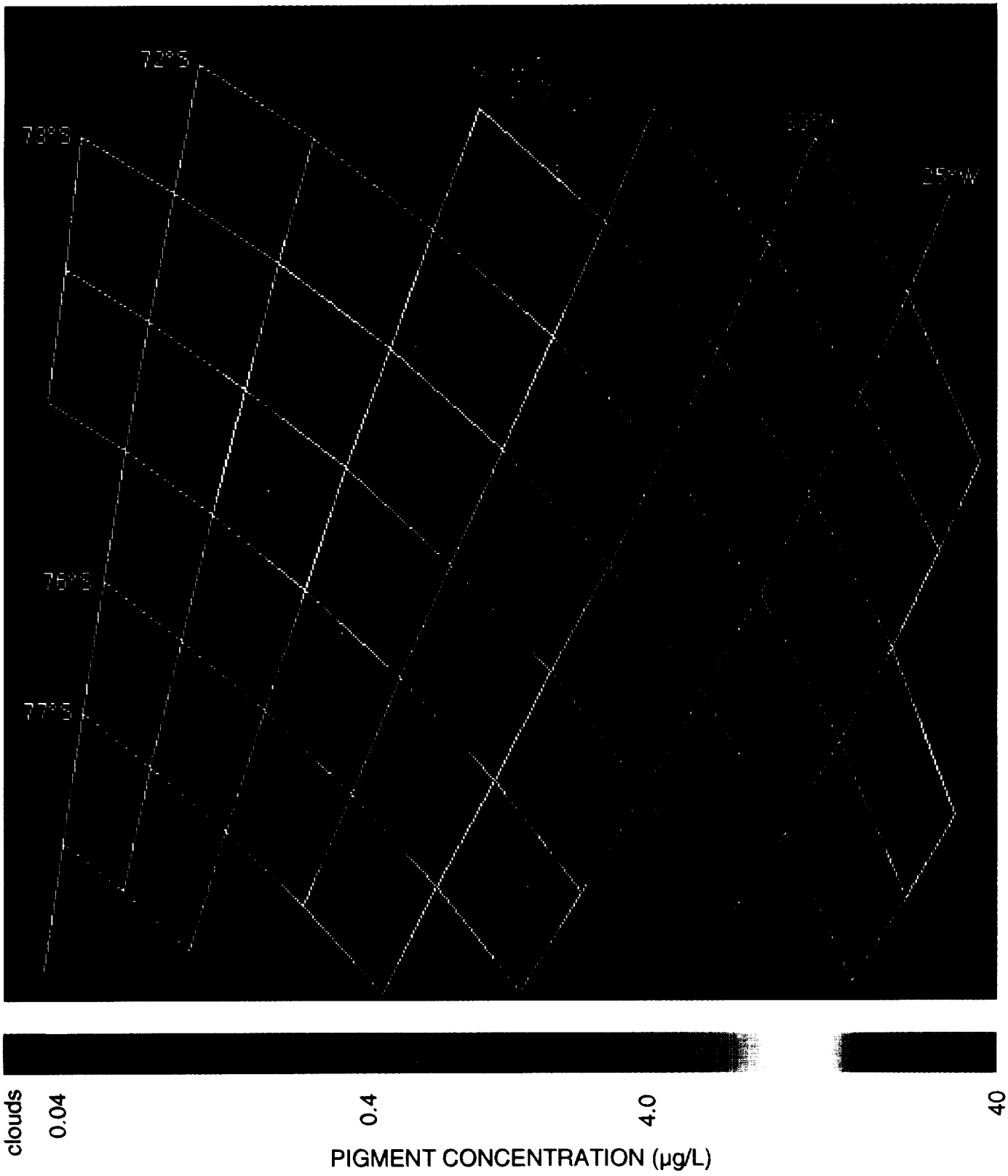

PLATE 2. Scene 1: CZCS pigment image from the western Weddell Sea for 1 March 1986. The image was processed assuming $\alpha_{750} = 0.7\%$, and using bilinearly interpolated surface pressure fields.

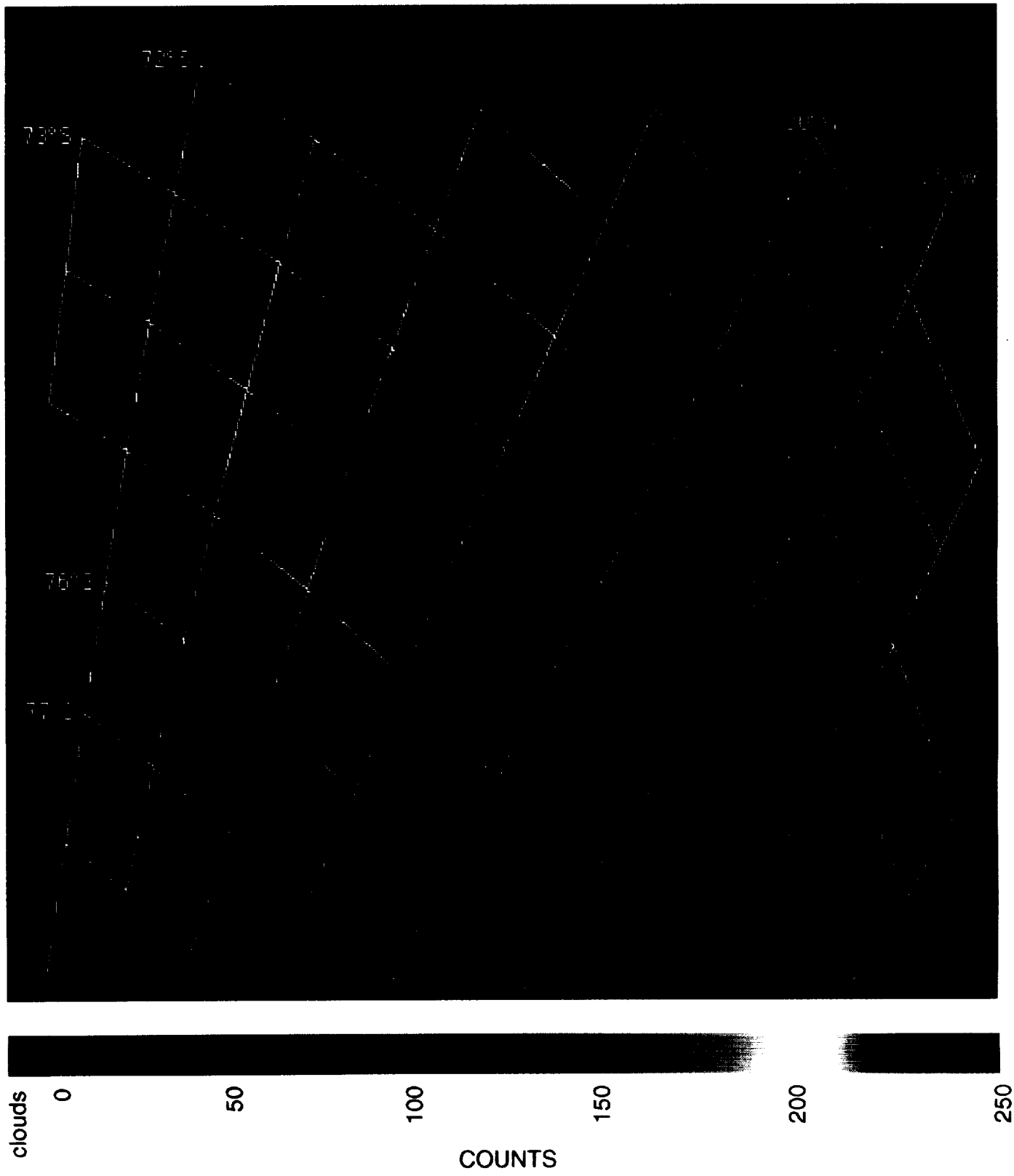

PLATE 3. The difference in computed pigments for scene 1 (processed assuming $\alpha_{750} = 0.7\%$) between the use of pixel-by-pixel variability in observed surface pressure, and using a spatially constant surface pressure of 1,013.25 mb.

PLATE 4. Scene 2: CZCS pigment image from the North Atlantic for 28 July 1980. The image was processed assuming $\alpha_{750} = 1.6\%$, and with a spatially constant surface pressure of 1,013.25 mb.

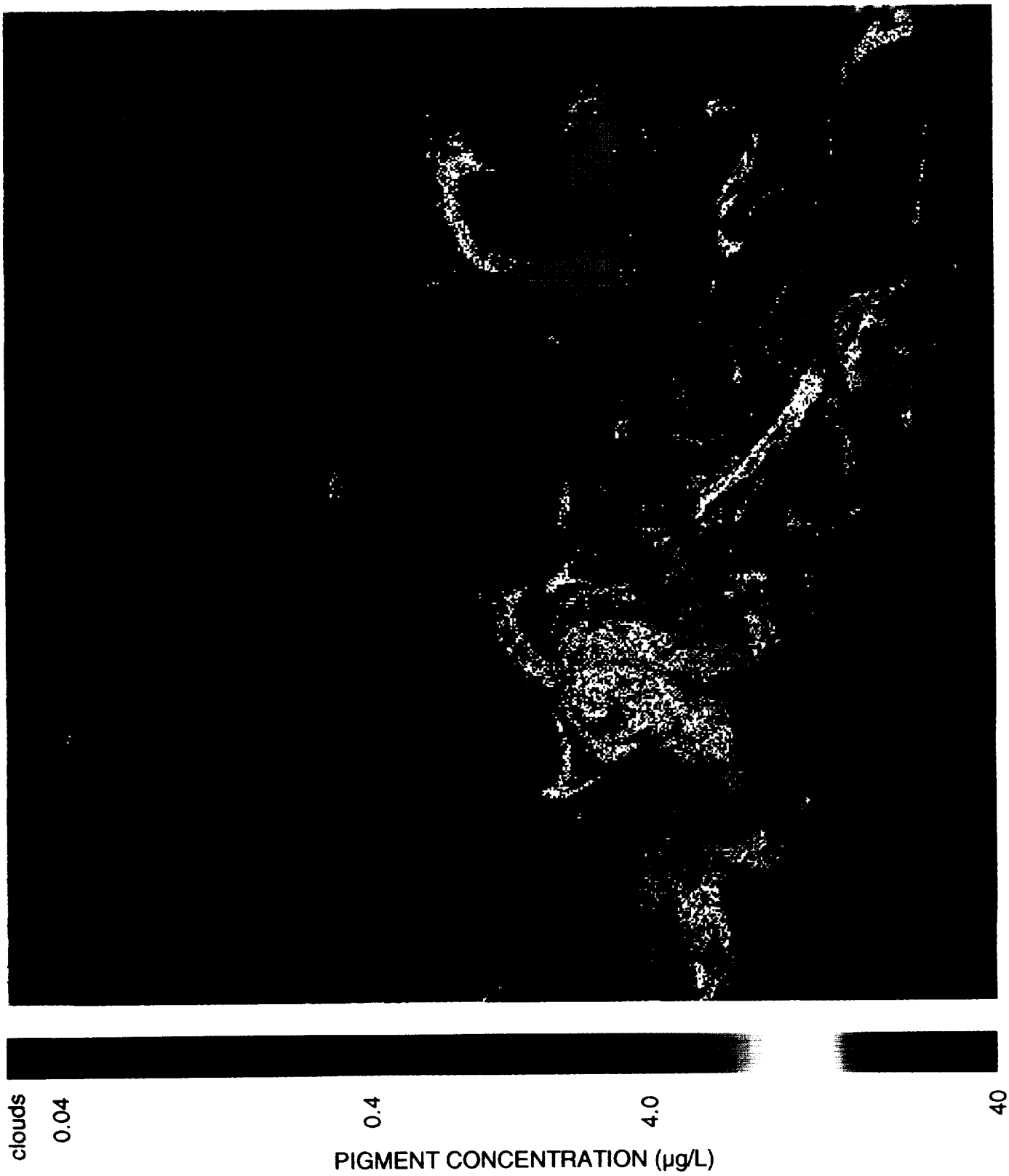

PLATE 5. Scene 2: CZCS pigment image from the North Atlantic for 28 July 1980. The image was processed assuming $\alpha_{750} = 0.7\%$, and with a spatially constant surface pressure of 1,013.25 mb.

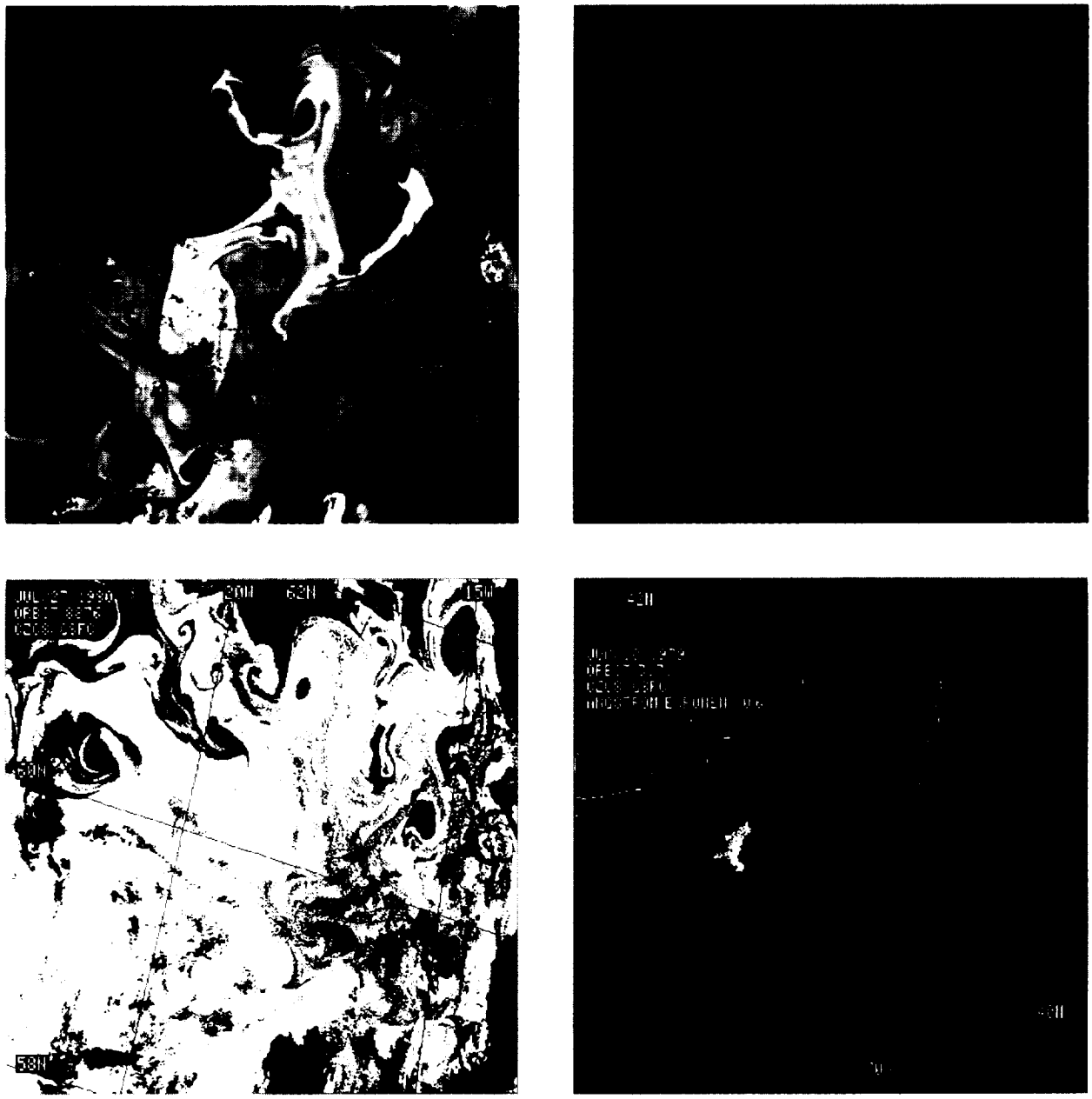

PLATE 6. In the top half of this plate, two true-color composites of coccolithophore blooms are shown. The left panel, a scene from CZCS orbit 8876, shows a bloom south of Iceland. The right panel, from CZCS orbit 3171, shows a bloom that occurred on the northeastern continental shelf of the US. The coccolithophore blooms are colored milky white. In the bottom half, the left panel shows the application of a coccolithophore bloom mask to the image shown at top left. The right panel shows the same mask applied to the image shown at top right. The coccolithophore mask is colored white and the non-bloom class is colored black.

REPORT DOCUMENTATION PAGE

Form Approved
OMB No. 0704-0188

1. AGENCY USE ONLY *(Leave blank)*	2. REPORT DATE	3. REPORT TYPE AND DATES COVERED
	May 1995	Technical Memorandum

4. TITLE AND SUBTITLE
SeaWiFS Technical Report Series
Volume 28–SeaWiFS Algorithms, Part 1

5. FUNDING NUMBERS
Code 970.2

6. AUTHOR(S) Charles R. McClain, Kevin R. Arrigo, Wayne E. Esaias, Michael Darzi, Frederick S. Patt, Robert H. Evans, James W. Brown, Christopher W. Brown, Robert A. Barnes, and Lakshmi Kumar
Series Editors: Stanford B. Hooker and Elaine R. Firestone
Technical Editor: James G. Acker

7. PERFORMING ORGANIZATION NAME(S) AND ADDRESS(ES)
Laboratory for Hydrospheric Processes
Goddard Space Flight Center
Greenbelt, Maryland 20771

8. PERFORMING ORGANIZATION REPORT NUMBER
95B00091

9. SPONSORING/MONITORING AGENCY NAME(S) AND ADDRESS(ES)
National Aeronautics and Space Administration
Washington, D.C. 20546–0001

10. SPONSORING/MONITORING AGENCY REPORT NUMBER
TM–104566, Vol. 28

11. SUPPLEMENTARY NOTES Michael Darzi, Frederick S. Patt, and Elaine R. Firestone: General Sciences Corporation, Laurel, Maryland; Robert H. Evans and James W. Brown: University of Miami, Miami, Florida; Christopher W. Brown: National Research Council, Washington, DC; Robert A. Barnes: ManTech Environmental Technology, Inc., Wallops Island, Virginia; and Lakshmi Kumar and James G. Acker: Hughes STX, Lanham, Maryland

12a. DISTRIBUTION/AVAILABILITY STATEMENT
Unclassified–Unlimited
Subject Category 48
Report is available from NASA Center for AeroSpace Information (CASI),
800 Elkridge Landing Road, Linthicum Heights, MD 21090; (301) 621-0390

12b. DISTRIBUTION CODE

13. ABSTRACT *(Maximum 200 words)*

This document provides five brief reports that address several algorithm investigations sponsored by the Calibration and Validation Team (CVT) within the Sea-viewing Wide Field-of-view Sensor (SeaWiFS) Project. This volume, therefore, has been designated as the first in a series of *algorithm* volumes. Chapter 1 describes the initial suite of *masks*, used to prevent further processing of contaminated radiometric data, and *flags*, which are employed to mark data whose quality (due to a variety of factors) may be suspect. In addition to providing the mask and flag algorithms, this chapter also describes the initial strategy for their implementation. Chapter 2 evaluates various strategies for the detection of clouds and ice in high latitude (polar and sub-polar regions) using Coastal Zone Color Scanner (CZCS) data. Chapter 3 presents an algorithm designed for detecting and masking coccolithophore blooms in the open ocean. Chapter 4 outlines a proposed scheme for correcting the out-of-band response when SeaWiFS is in orbit. Chapter 5 gives a detailed description of the algorithm designed to apply sensor calibration data during the processing of level-1b data.

14. SUBJECT TERMS
SeaWiFS, Oceanography, Algorithms,Control Masks, Flags, CZCS Imagery
Cloud Detection, Ice Detection, Coccolithophore Blooms, Ocean Color Imagery,
Correction Scheme, Sensor Calibration, Level-2 Processing

15. NUMBER OF PAGES
38

16. PRICE CODE

17. SECURITY CLASSIFICATION OF REPORT	18. SECURITY CLASSIFICATION OF THIS PAGE	19. SECURITY CLASSIFICATION OF ABSTRACT	20. LIMITATION OF ABSTRACT
Unclassified	Unclassified	Unclassified	Unlimited